Investigation of the Spatiotemporal Evolution of Tropical Cyclone Storm Surge under Sea Level Rise

Yi Liu

Dissertation submitted to the Faculty of the
Virginia Polytechnic Institute and State University
in partial fulfillment of the requirements for the degree of

Doctor of Philosophy
in
Civil Engineering

Jennifer L. Irish, Chair
Nina Stark
Pamela Murray-Tuite
Robert Weiss

June 12, 2018
Blacksburg, Virginia

Keywords: Storm Surge, Numerical Model, SWAN+ADCIRC, Sea Level Rise
Copyright 2018, Yi Liu

Investigation of the Spatiotemporal Evolution of Tropical Cyclone Storm Surge under Sea Level Rise

Yi Liu

(ABSTRACT)

Storm surges induced by tropical cyclones have been ravaging coastal communities worldwide, where a growing number of people reside. Tremendous life and economic losses are caused by tropical cyclones, contributing to more than half of the damages induced by natural hazards. To improve the resilience of coastal communities to surge hazards, it is of great importance to provide reliable and efficient real time forecasts of the spatiotemporal evolution of storm surge, as well as reliable predictions of the probabilistic surge hazards under future conditions. Three specific goals are addressed in this work. Studies on characterization and prediction of surge before a hurricane landfall show that a dimensionless relationship between intensity scaled surge magnitude and wind-duration scaled surge timing may effectively be used for rapid and reliable forerunner surge forecasting. Investigation of how probabilistic surge hazard changes with sea level rise (SLR) shows that the probabilistic surge with SLR can be 1.0 m larger, while different individual storm's surge with the same magnitude can be 1.5 m larger or 0.1 m smaller, indicating the importance of not relying on results from a limited number of storm surge events to assess the probabilistic surge hazard change to SLR. Finally, studying the temporal evolution of coastal flooding changes with SLR shows forerunner surge responds differently to SLR than peak surge, and that storm forward speed is a key factor determining the forerunner-SLR response.

Investigation of the Spatiotemporal Evolution of Tropical Cyclone Storm Surge under Sea Level Rise

Yi Liu

(GENERAL AUDIENCE ABSTRACT)

Flooding induced by tropical cyclones have been ravaging coastal communities worldwide, where a growing number of people reside. Tremendous life and economic losses are caused by tropical cyclones, contributing to more than half of the damages induced by natural hazards. To improve the resilience of coastal communities to flood hazards, it is of great importance to provide reliable and efficient real time forecasts of the flooding time series, as well as reliable predictions of the statistical flood elevation under future conditions. Three specific goals are addressed in this work. Studies on forecasting early coastal flooding show that a dimensionless relationship between storm characteristics and flood elevation may effectively be used for rapid and reliable early flood forecasting. Investigation of how statistical flood elevation changes with sea level rise show the importance of modeling the physical processes and of the storm sample size to address this issue. Finally, studying the coastal flooding time series with sea level rise shows early flooding responds differently to sea level rise, compared to maximum flooding, and that storm's moving speed is a key factor determining flooding response to sea level rise.

Acknowledgments

First and foremost, I want to express my heartfelt gratitude to Dr. Jennifer Irish. She has supported me by all means to help me become the independent researcher and confident science communicator that I am today. She guides me whenever I am confused, encourages me whenever I am frustrated, and inspires me whenever I hesitate. With her great wisdom and energy in research, Dr. Irish has always been a role model to me. In life, she has been nothing but completely supportive when I wanted to try different career choices. She gave me opportunities to write my own academic proposal, apply for my own funding, apply my research in engineering consulting, acquire teaching certificates, and teach my own class for a semester. Thank you Dr. Irish, for being so supportive and inspiring. I simply cannot imagine a better adviser.

I want to thank my committee, Dr. Robert Weiss, Dr. Nina Stark, and Dr. Pamela Murray-Tuite for their unconditional advising, critiques, and contributions to my dissertation work. What I haven learned from you is not only knowledge, but also one of the most precious traits in researchers - critical thinking ability.

I also want to thank my mentor and friend, Taylor Asher, for making research a fun thing to do. My gratitudes go to all the colleagues that have helped me along the way.

Thank you all my friends in Blacksburg and all around the world. Without your company and encouragement, this past five years would have been a much tougher journey for me. I want to especially thank my dancing buddies in Chaoxic for all the joys we have shared

together.

Last but not the least, thank you, mom and dad. Thank you, Jingren. No matter what path I have chosen and will choose down the road, I know you have been and will always be there for me.

Contents

List of Figures

List of Tables

Attribution

This dissertation adopts the Virginia Tech ETD manuscript format, where co-authors and affiliations are listed in the beginning of every manuscript chapter. In general, Jennifer Irish provided guidance and support through the process of data acquisition and analyses as the primary advisor. Irish edited all manuscripts and this dissertation. Taylor Asher helped with the simulations and analyses in Chapter 3, which he also edited as a co-author.

Chapter 1

Introduction

1.1 Significance

The Earth's coastlines have been witnesses to a continuously increasing human presence. More than 50% of the population now lives in the narrow stripes of coastal watershed in the US (NOAA, 2013). The thriving coastal communities have been constantly harassed by natural hazards, among which storm surge by tropical cyclones takes one of the leading roles, causing thousands of loss of lives and billions of dollars in economic damage (e.g, Hurricane Katrina (Knabb et al., 2005) and Typhoon Haiyan (Lagmay et al., 2015)). While the ability to predict peak surge is improving, less attention has been given to forerunner surge – a storm-induced early water surface elevation above mean sea level well in advance of a tropical cyclone landfall. As early as 1900, Galveston Texas was hit by a forerunner surge of 1.5 m 12 hours prior to storm landfall (Garriott, 1900). This forerunner surge flooded essential roadways and stranded many people on Galveston Island, directly contributing to the shocking death of 8000 people, making the 1900 Galveston Hurricane the deadliest hurricane on record (Blake et al., 2011). Since then, the occurrence of forerunner surge has been documented at different geographical areas, such as the upper Texas coast (Hurricane Ike (Kennedy et al., 2011)), the west Florida coast (Hurricane Dennis (Morey et al., 2006)), and the northwest Atlantic coast (Hurricane Sandy (Fanelli et al., 2013)) in the US, and the

west and south coasts of Australia (Eliot and Pattiaratchi, 2010).

Current research results are insufficient to quantify when, where and how large forerunner surges will be generated. Historically, literature has proposed two main hypotheses for the generation of forerunner surge. Well in advance of tropical cyclone landfall, the storm wind field is still parallel to the shoreline, making the physics of forerunner surge different from the physics of peak surge, which is largely induced by strong onshore wind. Bunpapong et al. (1985) considered the physics of the forerunner surge to be large seiching modes, which result from a sudden tropical cyclone entrance into the Gulf of Mexico. However, these seiching modes are usually in tens of centimeters, too small for the magnitudes of forerunner surges discussed here (1-2 m). Recently, Kennedy et al. (2011) investigated the forerunner surge as large as 2 m during Hurricane Ike from gauge data, and theorized that forerunner surge is in its nature Ekman setup. According to this hypothesis, a tropical cyclone with some distance from landfall presents a shore-parallel wind field, generating an alongshore current. This alongshore current is directed to the right in the Northern hemisphere under the influence of Coriolis force, creating a cross-shore pressure gradient that balances out this geostrophic effect, thus generating the Ekman setup. To test this hypothesis, Kennedy et al. (2011) used high-fidelity hydrodynamic numerical models to simulate the surge of Hurricane Ike and found that the forerunner surge of Ike disappeared without Coriolis force, concluding that Ekman setup does induce the forerunner surge. While the work of Kennedy et al. (2011) is considered as groundbreaking, their analysis was limited to one single historical tropical cyclone and based on hindcast of the wind and pressure fields, thus cannot be used for forerunner surge forecasting of any tropical cyclone.

More recently, Sebastian et al. (2014) used high-fidelity hydrodynamic numerical models to characterize tropical cyclone storm surge behavior within Galveston Bay. They also com-

pared surge results with and without Coriolis force, and proved that the physics of forerunner surge is Ekman setup. Based on Hurricane Ike, Sebastian et al. (2014) further varied the landfall location and the wind speed of the tropical cyclone to test different synthetic scenarios, i.e., artificially designed tropical cyclones, and discussed on how these different synthetic scenarios influence surge behavior. However, by only varying the wind speed and landfall location of a historical tropical cyclone, the complex variation of tropical cyclone meteorological conditions was not systematically considered. The storm track parameters of tropical cyclones include intensity (represented by pressure deficit Δp, related to wind speed), size (represented by pressure scale radii R_p), forward speed V_f, approach angle θ, and landfall location x. Hence, the study by Sebastian et al. (2014) did not consider the influence of other storm parameters like size R_p, forward speed V_f, and approach angle θ. More studies need to be conducted to find out the quantitative conditions under which significant forerunners can happen, and furthermore how forerunner surges respond to varying tropical cyclone storm track parameters in a systematic way.

While the magnitudes of the documented forerunner surges are usually in the range of 1-2 m, relatively small compared to peak surges, the increasing significance of predicting their timing and magnitudes cannot be overlooked with the impact of continuously rising sea levels and regional land subsidence. Based on satellite altimeter and in situ data, Church and White (2006, 2011) observed a global SLR rate of 1.7 ± 0.31 mm/year in the last century. Based on different greenhouse gas concentration trajectories, global mean SLR is projected to rise by 0.26 to 0.98 m by 2081-2100 (1986-2005 basis) with a 95% confidence interval (Church et al., 2013). Kopp et al. (2014) projected an even higher SLR of 1.2 m with a 90% probability by the end of this century (2000 basis). With maximum possible ice sheet loss considered, global SLR could be as high as 2.0 m by 2100 (1992 basis) (Rahmstorf, 2007; Vermeer and Rahmstorf, 2009; Parris et al., 2012). Regional SLR projections also

need to consider local factors that may counterbalance or exacerbate the SLR trend. For example, the eastern North Pacific coast has not experienced much SLR since 1980s because of impact from wind stress patterns and ocean circulation fluctuations (Bromirski et al., 2011). In contrast, relative sea levels along the coast of the Gulf of Mexico (especially the northwestern part) and the US Mid-Atlantic coast have been rising substantially due to land subsidence induced by glacio-isostatic adjustment, drainage, groundwater and oil withdrawal (González and Tornqvist, 2006; Mitrovica and Milne, 2002; Nicholls and Cazenave, 2010).

Meanwhile, it is also largely unclear how the probabilistic surge hazard, i.e., the surge value exceeded annually with a specific probability, will respond to sea level rise. An increased initial water elevation changes the hydrodynamics of storm surge. As a result, during the same tropical cyclone event, the difference between the water elevation with SLR (ζ_{SLR}) and the water elevation without SLR (ζ_0) adding with the magnitude of SLR (λ) does not always equal to zero. For example, a coastal city with a 1% annual exceedance probability (AEP) surge value of 1 m nowadays may experience a 1% AEP surge of 2.5 m or 1.5 m instead of 2 m in the future with a 1 m SLR, with respect to the same vertical datum.

To better inform coastal planning and flood mitigation development, more studies are needed to address where the SLR-induced probabilistic surge hazard changes happen and the physical drivers behind these changes. Researchers have been using numerical models to dynamically simulate tropical cyclones with SLR imposed on initial sea surface to study the surge-SLR response. For example, Smith et al. (2010) simulated six storms under three SLR scenarios (0.0 m, 0.5 m, 1.0 m) for Southeast Louisiana using surge and wave models, and concluded that individual surge value does change with SLR. According to Smith et al. (2010), the surge levels could be increased by as much as 1-3 m in addition to SLR in part of the study area. Bilskie et al. (2014) used similar model setup in the same area with additional

consideration of land use land cover change induced by SLR, and also found that individual surge response to SLR was dynamic and sensitive to landscape changes. Because the high-fidelity hydrodynamic models used in these studies are computationally expensive, most of these studies used a limited number of tropical cyclones that were believed to produce surge values of a specified AEP as illustrative examples. A different approach was adopted by Lin et al. (2012), where 2000 synthetic storms were simulated and a more strict evaluation of surge probabilities under climate change was conducted. However, to enable the large number of simulations for probability evaluation, Lin et al. (2012) used a low-fidelity model setup and only considered tidal effects nonlinearly. SLR was assumed to linearly affect the probabilistic surge hazard.

1.2 Research Goals

Building upon the aforementioned literatures, the work presented in this dissertation aims to further investigate the spatiotemporal evolution of tropical cyclone storm surge under sea level rise scenarios. Based on the prevalence of surge hazards and the rates of SLR, considering the effects of different geographical locations, study areas include upper Texas coast, west Florida coast, and northwest Atlantic coast. Specifically, three research questions are addressed by testing each corresponding hypothesis in the following chapters.

Research Question 1 (RQ1): *How do different physical processes (e.g., wind setup, wave setup, Ekman setup induced by Coriolis force) trade off over the spatiotemporal evolution of storm surge?*

Hypothesis 1: We hypothesize that different physical processes, including wind setup, Ekman

setup, wave setup and tides dominate different temporal component of tropical cyclone storm surge. For example, it is already known that wind setup caused by strong onshore wind usually dominates the peak surge, and some evidence has shown that Ekman setup induced by Coriolis force dominates the forerunner surge of Hurricane Ike (Kennedy et al., 2011). We further hypothesize that Ekman setup generally dominates the forerunner surge for any tropical cyclone in the study areas, assuming effects of the other physical processes such as wave setup and tides are small.

Research Question 2 (RQ2): *How does varying meteorological forcing influence the spatiotemporal evolution of storm surge?*

Hypothesis 2: We hypothesize that the timing and magnitude of forerunner surge are closely related to storm track parameters (intensity represented by pressure deficit Δp, size represented by pressure scale radii R_p, forward speed V_f, approach angle θ, and landfall location x_0), and further hypothesize that this relationship can be quantified based on high-fidelity numerical surge modeling results.

Chapter 2 presents studies testing Hypotheses 1 and 2 in Virginia, New York/New Jersey, and Texas. Results show that Ekman setup does dominate the forerunner surges of the tropical cyclones in these three study areas. Based on the physics of Ekman setup and a dimensional analyses on the shallow water momentum equation, a dimensionless relationship between central-pressure scaled surge and wind-duration scaled time may effectively be used for rapid forerunner surge forecasting with uncertainties considered.

Research Question 3 (RQ3): *How and why does the spatiotemporal evolution of storm surge respond differently to sea level rise?*

Hypothesis 3: We hypothesize that the spatial pattern of peak surge as well as the probabilis-

tic surge hazard will change under the influence of SLR, and that trend in these changes can be captured considering their physical drivers. We also hypothesize that different temporal component of storm surge (e.g., forerunner surge, peak surge) responds differently to the same SLR scenario.

Chapter 3 investigates the physical drivers of changes in probabilistic surge hazard under sea level rise in Tampa Bay region of West Florida. It is found that when considering higher SLR scenario, regions with wider openings for piling up surge water with limited drainage paths, and/or large surge events, surge is expected to respond more nonlinearly and less predictably to SLR; and thus should be examined more closely to guide future planning, engineering, and mitigation measures.

Chapter 4 presents results about impact of sea level rise on the temporal evolution of storm surge. Results show that temporal evolution of storm surge responds differently to sea level rise for storms with different forward speed at regions with different topographic features.

Finally, a comprehensive conclusion is included in Chapter 5.

Chapter 2

Characterization and Prediction of Tropical Cyclone Forerunner Surge

Yi Liu[1], Jennifer L. Irish[1]

[1]Department of Civil and Environmental Engineering, Virginia Tech, Blacksburg, VA, USA

Under Review at Coastal Engineering.

Abstract

Forerunner surge, a water level rise ahead of tropical cyclone landfall, often strikes coastal communities unexpectedly, stranding people and increasing loss of life. Surge forecasting systems and emergency managers almost exclusively focus on peak surge, while much less attention is given to forerunner surge. To address the need for fast and accurate forecasting of forerunner surge, we analyze high-fidelity surge simulations in Virginia, New York/New Jersey and Texas and extract physical scaling laws between readily available storm track information and forerunner surge magnitude and timing. We demonstrate that a dimensionless relationship between central-pressure scaled surge and wind-duration scaled time may effectively be used for rapid forerunner surge forecasting, where uncertainty is considered. We use our method to predict forerunner surge for Hurricanes Ike (2008)—a significant forerunner surge event—and Harvey (2017). The predicted forerunner surge 24 to 6 hours before Hurricane Ike's landfall ranged from 0.4 to 2.8 m, where the observed forerunner surge ranged from 0.4 to 2.6 m. This new method has the potential to be incorporated into real-time surge forecasting systems to aid emergency management and evacuation decisions.

2.1 Introduction

Tropical cyclone (TC) storm surge has had devastating impacts on coastal communities worldwide, causing tremendous loss of life and physical damage. Peak surge is most often the dominant driver of direct damage. Consequently, surge forecasting systems and emergency managers have focused on improving prediction of peak surge, while less attention has been given to forecasting forerunner surge—a storm-induced early water level rise above mean sea level well in advance of TC landfall. The significance of forerunner surge was first observed in 1900, when Galveston, Texas was hit by a forerunner surge of 1.5 m 12 hours prior to landfall (Garriott, 1900; Kennedy et al., 2011) . This forerunner surge flooded essential roadways and stranded many people on Galveston Island, directly contributing to the shocking death of 8,000 people, and making the 1900 Galveston Hurricane the deadliest hurricane on record (Blake et al., 2011). Forerunner surge is most dangerous for those who are in the direct path of the cyclone, where the forerunner surge precedes a high peak surge. Significant forerunner surges occurred in 1900 and again in 2008 (Hurricane Ike) when these storms made landfall in Galveston. Since 1900, forerunner surge on the order of 1 to 2 m has been documented for TCs impacting both the US Gulf of Mexico and Atlantic coasts (Table 2.1). Yet, while a few studies indicated that large TCs making landfall across a broad, shallow continental shelf could potentially generate significant forerunner surges (Kennedy et al., 2011; Sebastian et al., 2014)—where Kennedy et al. demonstrated Hurricane Ike's large forerunner surge was predominantly from Ekman setup (water level rise arising from the influence of Coriolis force)—we lack a basic quantitative understanding of how and when significant forerunner surge is generated.

To better inform evacuation plans and thereby reduce loss of life, it is important to understand the conditions in which a TC generates significant forerunner surge. Surge forecasts

Table 2.1: Historical TCs with recorded forerunner surges (12 hours before landfall). Data source: (a) Garriott (1900), (b) Stewart (1915), (c) Kennedy et al. (2011), (d) NOAA (2017), (e) Cline (1920), and (f) Fanelli et al. (2013).

Tropical Cyclone	Area	Forerunner Surge (m)
Unnamed, 1900	Galveston, TX	$1.5^{(a)}$
Unnamed, 1915	Galveston, TX	$2.1^{(b)}$
Ike,2008	Galveston, TX	$1.8\text{-}2.0^{(c)(d)}$
Unnamed, 1915	Tampa, FL	$1.5^{(e)}$
Sandy, 2012	Norfolk, VA	$1.0^{(f)}$

historically focus on the rapid and accurate prediction of peak surge, and due to the need for rapid forecasting, either use a large ensemble set of track possibilities with low-fidelity surge simulations (e.g., NOAA's P-Surge (Glahn et al., 2009; Taylor and Glahn, 2008)), use a small, discrete set of storm track possibilities with high-fidelity surge simulations (e.g., (Dietrich et al., 2013)), or use interpolation schemes to determine peak surge from discrete, high-fidelity simulations for a large ensemble of track possibilities (e.g., (Irish et al., 2011b; Taflanidis et al., 2013)). Some rapid surge prediction methods also consider forecasting of surge time series, where either accuracy was compromised (Jia et al., 2016) or interpolation schemes were used [10]. Forerunner surge is often overlooked when considering real-time forecasts.

Herein, to advance the physical understanding of forerunner surge generation and provide a reliable and rapid forerunner surge forecasting method, we examine time series from high-fidelity storm surge simulations for Galveston, TX, Hampton Roads, VA, and New York/New Jersey, and we characterize forerunner surge magnitude and timing using physical scaling laws based on storm track parameters.

2.2 Methods

The forerunner surge observational record is sparse, both in terms of the number of cyclones observed and in spatiotemporal coverage, so we base our analysis on simulated wind, barometric pressure, and surge for a range of synthetic TCs representative of observed storm characteristics (Landsea et al., 2008). Here, the unstructured finite-element shallow water equations code ADCIRC (Luettich et al., 1992) is used, coupled with a spectral wave model (e.g., SWAN (Booij et al., 1996) or STWAVE (Smith et al., 2001)) to include the effects of wave setup (Dietrich, 2011; Dietrich et al., 2012). Runup from individual waves is not included. TC wind and pressure fields are generated from a planetary boundary layer (PBL) model (Thompson and Cardone, 1996), using storm track parameters as input, including storm position, central pressure deficit (Δp) representing intensity, radii to maximum wind (R) representing storm size, forward speed (V_f), heading ( ), and profile parameter Holland B (Holland, 1980). Our focus herein is on characterizing the forerunner surge anomaly (level above expected normal level). To simplify the analysis, astronomical tides are not considered.

We conduct dimensional analysis on the simulations to find physical scaling laws relating surge timing and magnitude to storm track parameters 12 to 24 hours before landfall. Former studies have shown that the storm parameters most influencing the magnitude of peak surge are landfall location (x_o), Δp, and R, while V_f and θ have less impact (Irish et al., 2008). In this forerunner surge study we also focus on the storm parameters Δp and R. However, we identify through sensitivity analyses that V_f also significantly influences forerunner surge, while heading and landfall location have less impact. Specifically, while landfall location (x_0) is known to strongly influence peak surge (Irish et al., 2009), our sensitivity analysis indicates forerunner surge (represented by surge 12 hours before landfall) is not very sensitive to moderate shifts in track, especially at the open coast. At location TX-2 in Figure 2.1,

as an example, our simulations exhibit differences in forerunner surge magnitude 12 hours before landfall of less than 0.1 m, when track spacing is varied up to 35 km, and when all other storm parameters are held constant. Field observations also support this conclusion (see Appendix A, Figures A.2 to A.7). When track is varied up to 200 km to the south of Houston/Galveston (Figure A.1), forerunner surge is generated, but its magnitude does not change significantly, less than 0.2 m. Storms tracking 100 km or more to the north, northeast of Houston/Galveston do not generate forerunner surge; Houston/Galveston is well to the left of the hurricane eyewall for these storms, which thus result in strong offshore winds in the study area. A sensitivity test is also conducted in terms of storm heading (θ), and results show little difference between storms with different headings (less than 0.1 m increase over a heading change of ± 45 degrees at location TX-2), although results in the bay can be more complicated due to locally generated surge—a process not directly considered herein.

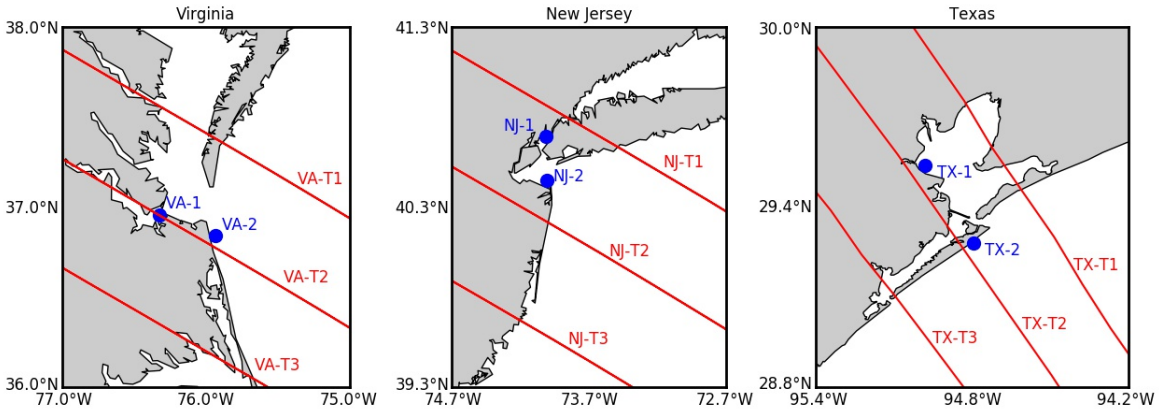

Figure 2.1: Maps of Virginia, New York/ New Jersey, and Texas coasts with synthetic TC tracks and representative study locations. VA-1 and VA-2 are locations at Sewells Point and Virginia Beach, respectively. TX-1 is within Galveston Bay and TX-2 is near Galveston. NJ-1 and NJ-2 are locations near The Battery and Sandy Hook.

Thus, for each region we consider just one heading, a limited range of x_o (where forerunner surge precedes a peak along-coast surge occurring near the study location), and a wide range of Δp,R and V_f. We leverage existing surge simulations for Virginia and New York/New

Jersey and perform our own simulations for Texas. In Virginia and New York/New Jersey, we use the US Army Corps of Engineers (USACE) STWAVE+ADCIRC simulations (Cialone et al., 2017). For this study, 19 synthetic TCs along three tracks making landfall in or near Hampton Roads are selected (Figure 2.1). All storms follow headings of −60 degrees clockwise from north. Track parameters Δp, R, and V_f are respectively varied from 38 to 88 hPa, 25 to 109 km, and 3.3 to 12.2 m/s at landfall. Results are shown for two representative locations near densely populated areas: Sewells Point (VA-1) within Chesapeake Bay and Virginia Beach (VA-2) on the open coast. Similarly, 18 synthetic TCs along three tracks in or near Sandy Hook, NJ are selected, with headings of -60o and track parameters Δp, R, and V_f varying from 28 to 78 hPa, 31 to 139 km, and 6.7 to 18.6 m/s at landfall. Results are shown for two representative locations near densely populated areas: The Battery, NY (NJ-1) and Sandy Hook, NJ (NJ-2).

In Texas, we simulate surge using SWAN+ADCIRC, employing Dietrich et al. (2012) validated high-resolution computational mesh and model setup used in Kennedy et al. (2011) forerunner surge study. We first assess model performance using a synthetic TC similar to Hurricane Ike in terms of these track parameters: Δp of 63 hPa, R of 74 km, and V_f of 18 km/h at landfall (Berg, 2009; Sebastian et al., 2014). Wind and pressure forcing are developed using the PBL model. It should also be noted that herein we define the forerunner surge generally as the water level rise ahead of TC landfall, for the purposes of this paper the surge time series during the period from 24 to 6 hours prior to landfall. With this definition, the forerunner surge encompasses Ekman setup as well as other processes inducing surge prior to landfall. This simulation is compared both with Kennedy et al. (2011) observations and simulation using the best available observation-based H*Wind wind field (Figure 2.2). Some differences exist between observations and our model results using parameterized wind forcing, and most of these cannot be eliminated, even when using the observation-based H*Wind

forcing. Repeating Kennedy et al.'s analysis, our surge simulation using parameterized winds when Coriolis force is disabled shows that the major part of Ike's forerunner surge indeed does arise from Ekman setup, and is captured when using the parameterized wind field. Note that the simulated surge time series herein do not show a forerunner peak that is observed during Hurricane Ike, and we think this arises for two reasons. First, although using a best wind field hindcast will certainly provide a more accurate simulated estimate with a forerunner peak, we purposefully elect to use parameterized wind fields because we want our results to be useful for forecasting purposes. Second, we hypothesize that the depth-averaged model underestimates the current speed of importance to forerunner surge (that in the upper ocean layer), thus underestimating the forerunner peak. This underestimate is also see in the simulations using H*Wind. Thus, although exhibiting some error, the synthetic storm surge simulations analyzed herein can be used to assess trends in forerunner surge as a function of real-time forecasted storm track parameters.

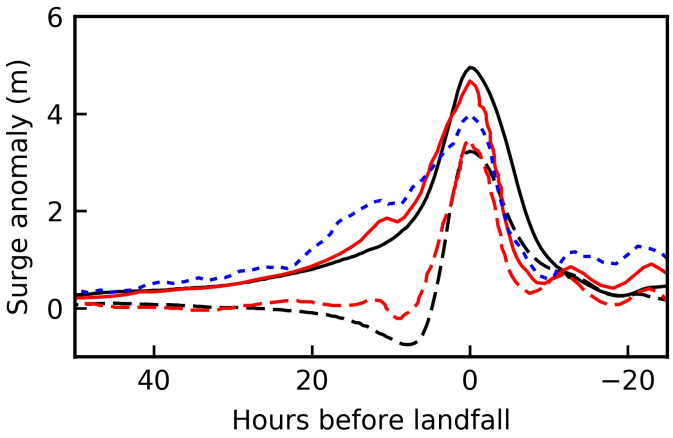

Figure 2.2: Surge time series validation for Hurricane Ike (2008) at location TX-2 in Figure 2.1. Black lines: model results with parameterized wind (PBL); red lines: model results with best reconstructed wind (H⋆wind); solid lines: model results with Coriollis force; dashed lines: model results without Coriollis force; dotted line: observations. Dotted and dashed lines are observations and simulations from Kennedy et al. (2011).

In Texas, we simulate surge for synthetic TCs along three tracks spaced 35 km apart and

making landfall in or near Galveston (Figure 2.1). All storms follow tracks oriented -30o clockwise from north. Along the middle track (TX-T2), 42 combinations of Δp, R and V_f are simulated, respectively spanning from 53 to 113 hPa, 10 to 85 km, and 3 to 12 m/s at landfall. These 42 simulations reveal trends consistent with those seen in the Virginia simulations, so a reduced set of 19 TCs are simulated for the north (TX-T1) and south tracks (TX-T3). In all 80 unique storm simulations are considered in Galveston. Results are shown for two representative locations near densely populated areas, Houston (TX-1) within Galveston Bay and Galveston (TX-2) on the open coast. Selected storms are simulated without Coriolis forcing in order to confirm the prominent role of Ekman setup in forerunner surge generation (Figure A.8).

2.3 Results and Discussion

To identify the relative influence of each storm parameter on forerunner surge, we investigate correlation between the forerunner surge magnitude and storm parameters. At 12 hours prior to landfall, for example, partial correlation coefficients for Δp, R, and V_f are respectively 0.52, 0.82, and -0.87 for Virginia, 0.71, 0.86, and -0.73 for Texas, and 0.56, 0.68, and -0.83 for New York/New Jersey. As Δp and R increase, so do forerunner surge (shown herein) and peak surge (Irish et al., 2008). In contrast, while increasing V_f tends to increase peak surge somewhat (Resio et al., 2009), it serves to decrease forerunner surge magnitude. This result is expected considering the physics of forerunner surge demonstrated in Kennedy et al. (2011) that shows strong wind-generated alongshore currents on the continental shelf produce Ekman setup (ζ_{Ek}) under the effect of Coriolis force. Approximated from the cross-shore

momentum balance, Ekman setup is:

$$\zeta_{Ek} = \int \frac{fU}{g} dx \tag{2.1}$$

where f is the Coriolis coefficient, U is alongshore water current speed, g is gravitational acceleration, and x is in the cross-shore direction. The factors controlling timing and magnitude of forerunner surge are the alongshore-current speed and the cross-shore width of the current (Equation 2.1's integration limit). Figure 2.2 shows simulated surge time series, where each storm is colored based on the dimensional parameter $(\frac{R}{V_f})(\Delta p)$ to reflect the positive correlation with Δp and R and negative correlation with V_f. Results show that for the parameter range simulated, the forerunner surge magnitude ranges from 0.0 to 2.0 m between 24 and 6 hours before landfall, in both Virginia and Texas. As expected, surge increases in magnitude closer to landfall. The results further show larger $(\frac{R}{V_f})(\Delta p)$ results in larger forerunner surge. The interpretation is twofold. First, (R/V_f) represents the duration in which strong cyclonic winds persist over the continental shelf. The longer the wind field lingers in this relatively shallow-depth region, the more time it has to fully develop an alongshore water current. Second, Δp represents overall wind-field intensity. All else being equal, a more intense TC generates a more intense wind field, which in turn induces a stronger alongshore current.

To take a step further, we use dimensional analysis to develop physical scaling laws relating forerunner surge and storm track parameters near landfall. The forerunner surge magnitude and timing are scaled by Δp and (R/V_f) respectively. A region-specific characteristic intensity (Δp_{char}) and characteristic duration (t_{char}) are further integrated into the scaling to

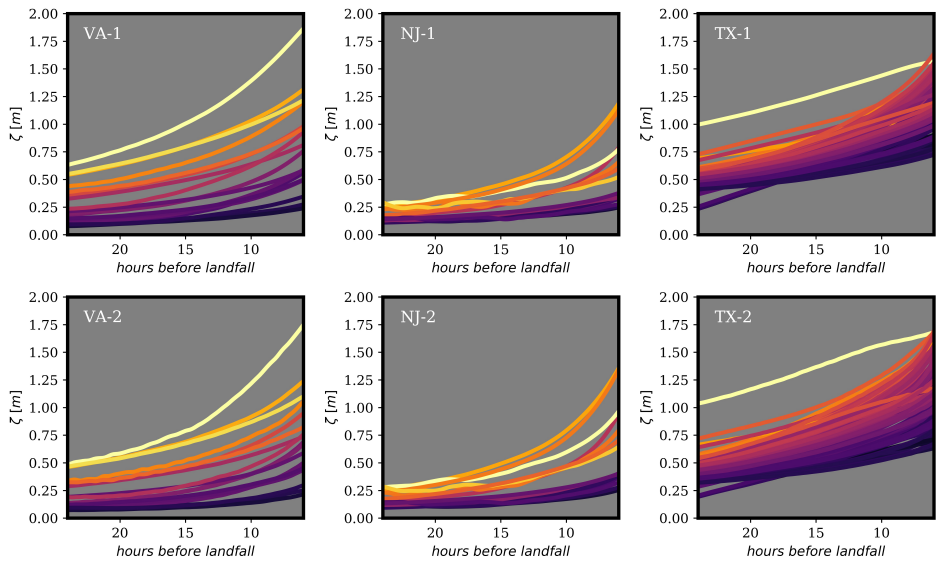

Figure 2.3: Surge time series of 19 simulations in Virginia, 18 simulations in New York/New Jersey and 80 simulations in Texas. Timing is defined as hours before storm landfall. Plots are colorized by $(\Delta p)(\frac{R}{V_f})$, where lighter colors represent larger values.

account for regional characteristics. Thus,

$$\begin{cases} \zeta\prime = (\dfrac{\gamma\zeta}{\Delta p})(\dfrac{\Delta p_{char}}{\Delta p}^{\alpha}) & \text{(2.2a)} \\ t\prime = (\dfrac{t}{R/V_f})(\dfrac{t_{char}}{R/V_f})^{\alpha} & \text{(2.2b)} \end{cases}$$

where γ is the specific weight of seawater, t is time before peak surge on the open coast, and ζ is surge magnitude. The quantity $\frac{\gamma\zeta}{\Delta p}$ in Equation 2.2a is derived from the momentum balance, where Δp is considered proportional to surface wind stress in a quadratic form ($\Delta p \propto u^2_{wind}$)(Irish et al., 2009; Irish and Resio, 2013), and the quantity $(\frac{t}{R/V_f})$ in Equation 2.2b represents wind duration. The term Δp_{char} is regional mean observed central pressure deficit, $58hPa$ in Virginia and New York/New Jersey, and $62hPa$ in Texas. The term t_{char}) is defined as $\frac{L_{shelf}}{\sqrt{g\bar{h}_{shelf}}}$, where L_{shelf} is reference continental shelf width, taken as distance from the coastline to a depth of $100m$, and $\bar{h}_{shelf}$is reference shelf depth, taken as $50m$. The term L_{shelf} represents the Ekman setup integration limit and $\sqrt{g\bar{h}_{shelf}}$ represents a characteristic

speed of a free wave on the shelf. The best-fit coefficient α is site-specific. Taken as 0 in Virginia, -0.35 in Texas, and -0.35 in New York/New Jersey, α is thought to arise from the effect of a curved coastline on Ekman setup. Specifically, we hypothesize the concave coastline curvatures of the Galveston and New York/New Jersey regions redirect and confine the driving alongshore current, while, the Hampton Roads region's convex coastline curvature has less influence on the alongshore current. After scaling, Equation 2.2a represents the dimensionless surge $\zeta\prime$ and Equation 2.2b represents the dimensionless timing $t\prime$ of forerunner surge. By plotting the time series in this dimensionless space in Figure 2.3, the surge simulations at each location collapse into a hyperbolic curve. Thus,

$$\zeta\prime = \frac{a}{t\prime + b} + c \tag{2.3}$$

where a, b, and c are site-specific curve fitting coefficients Table A.2 that we hypothesize are related to local factors, such as continental shelf width, latitude, and bathymetry.

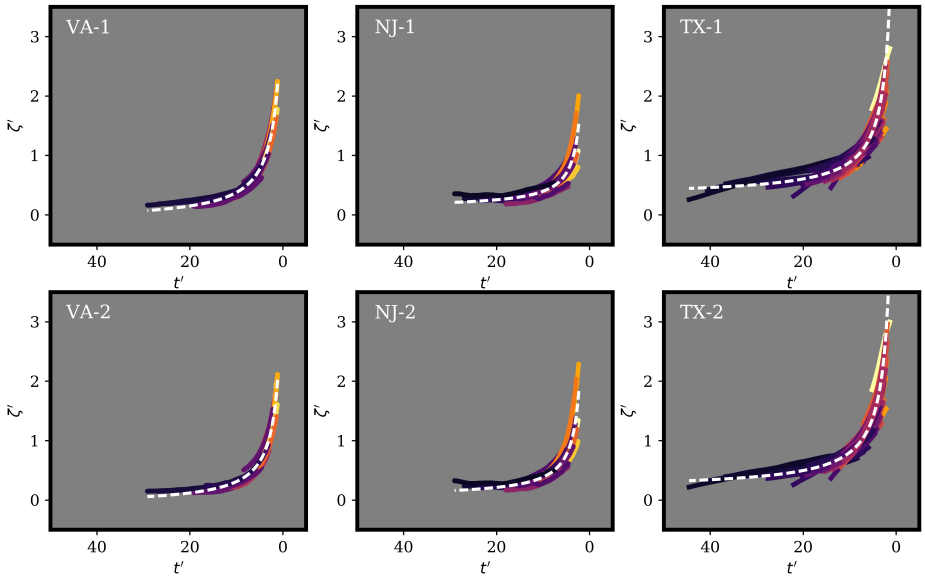

Figure 2.4: Plots of dimensionless surge ($\zeta\prime$) versus dimensionless time ($t\prime$) at representative locations. Plots are colorized by $(\Delta p)(\frac{R}{V_f})$, where lighter colors represent larger values. The dashed white lines represent fitted hyperbolic curves.

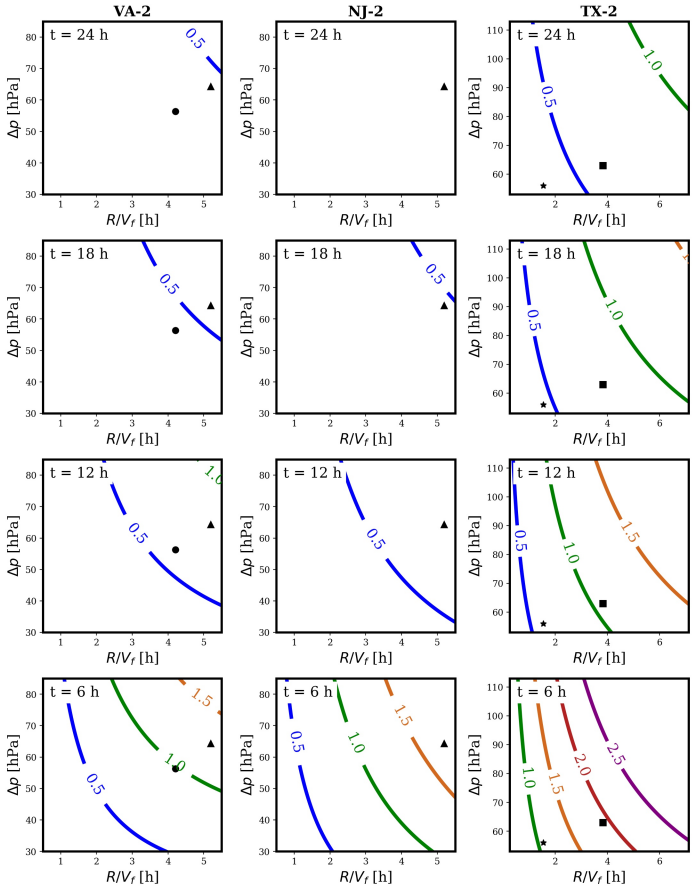

Figure 2.5: Deterministic forerunner surge forecasts at VA-2 (Virginia Beach) NJ-2 (Sandy Hook), and TX-2 (Galveston) at 24, 18, 12 and 6 hours before TC landfall, with Hurricanes Isabel (2003, circles), Ike (2008, squares), Sandy (2012, triangles), and Harvey (2017, stars) imposed. The 6-hr Sandy value at NJ-2 is extrapolated beyond the dimensionless data limits.

Uncertainty associated with this time-evolving surge response function Equations 2.2 and 2.3 arises from two primary sources. First, these equations are based on high-fidelity synthetic storm surge simulations. Thus, uncertainties related to parameterization of the wind fields, surge, and wave model assumptions, are carried into the scaling. Based on comparing observations and high-fidelity surge simulations for eight historical hurricanes (US Atlantic coast: Sandy [2012], Irene [2011], Isabel [2003], Gloria [1985], Josephine [1984]; US Gulf of Mexico coast: Ike [2008], Katrina [2005], and Rita [2005]) (Bunya et al., 2010a; Cialone et al., 2015), this uncertainty is found to increase linearly as surge magnitude increases (Figure 2.7). Sec-

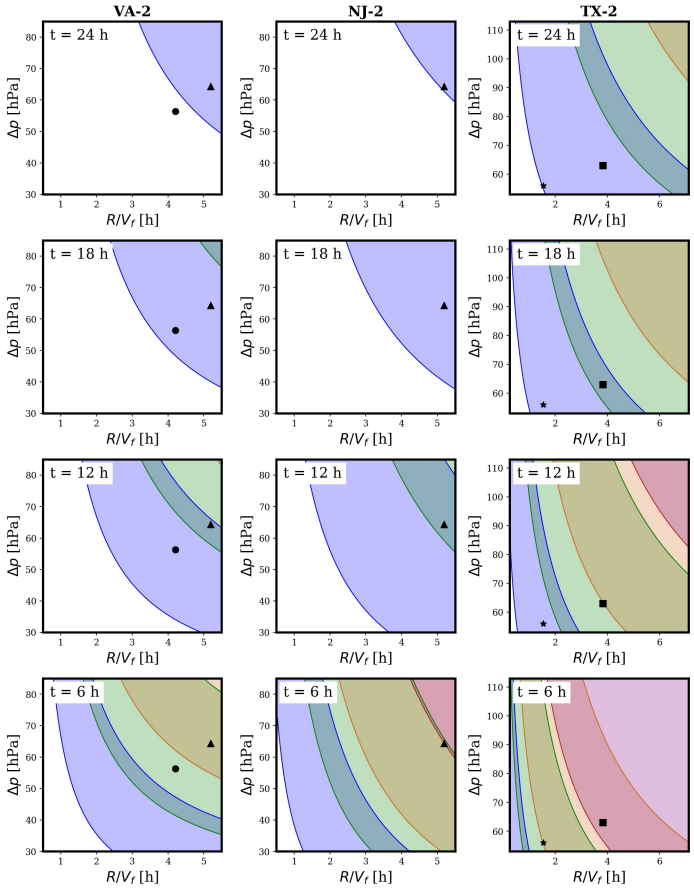

Figure 2.6: Forerunner surge forecasts with uncertainty bands at VA-2 (Virginia Beach) NJ-2 (Sandy Hook), and TX-2 (Galveston) at 24, 18, 12 and 6 hours before TC landfall, with Hurricanes Isabel (2003, circles), Ike (2008, squares), Sandy (2012, triangles), and Harvey (2017, stars) imposed. Blue, green, orange and purple correspond to 0.5 m, 1.0 m, 1.5 m, and 2.5 m respectively. The 6-hr Sandy value at NJ-2 is extrapolated beyond the dimensionless data limits.

ond, uncertainty arises from the curve fitting process, and is also found to scale linearly with surge magnitude (Figure 2.7). Thus, as a measure of uncertainty, total standard deviation of the time-evolving surge response function σ_{tot} is:

$$\begin{cases} \sigma_{tot}^2 = \sigma_{model}^2 + \sigma_{function}^2 & \text{(2.4a)} \\ \sigma_{model}, \sigma_{function} = (k)(\zeta) + l & \text{(2.4b)} \end{cases}$$

where σ_{model} is the standard deviation of wind and surge simulations, $\sigma_{function}$ is the standard

deviation of surge prediction calculated by Equations 2.2 and 2.3 compared to the simulated results, ζ is forerunner surge magnitude at different times, and k and l are linear regression coefficients. Uncertainty in predicting the timing of forerunner arrival is also quantified as the average prediction uncertainty for observed forerunner surges ranging from 0.3 to 2.0 m (Figure 2.8). With uncertainty considered, Equations 2.2 and 2.3 may be used to rapidly predict forerunner surge for a specific storm, as well as to determine the likelihood of the occurrence of storms with potential to generate significant forerunner surge. As an example, Figures 2.5 and 2.6 shows forerunner surge at 24, 18, 12, and 6 hours before landfall at Virginia Beach (VA-2), Sandy Hook (NJ-2), and Galveston (TX-2), where surge is calculated as ζ in Figure 2.5 and $\zeta \pm \sigma_{tot}$ in Figure 2.6 using Equations 2.2 to 2.4.

Within the range of storm track parameters considered, a forerunner surge of 1 m or more generally occurs earlier than 12 hours before landfall. Using track parameters Table A.1, we predict that 12 hours before landfall, the forerunner surge at Virginia Beach is 0.4-0.9 m during Hurricane Isabel (2003), which made landfall about 200 km to the south, and is consistent with an observed value of 0.5 m at the Sewells Point NOAA station ((NOAA, 2017); Figure A3). Hurricane Sandy (2012) made landfall about 100 km to the south of Sandy Hook, where we predict the forerunner surge 12 hours before landfall is 0.4-1.1 m. The observed value here was 1.2 m ((NOAA, 2017); Figure A4). We hypothesize that the slight underestimation is due to the long hovering of Sandy's enormous wind field on the continental shelf before it changed direction to make landfall. In Galveston, we predict Hurricane Ike's (2008) forerunner surge 24, 18, 12 and 6 hours before landfall is 0.4-0.9 m, 0.5-1.1 m, 0.7-1.6 m, and 1.2-2.8 m, where observed value was respectively 0.7 m, 1.1 m, 1.8 m, and 2.6 m at the Galveston Pier 21 NOAA station ((Kennedy et al., 2011; NOAA, 2017); Figure A6). The predicted arrival for a 1.0-m forerunner during Ike is 14±7 hours before landfall (Figure S12, S13), where the observed arrival was 20 hours before landfall

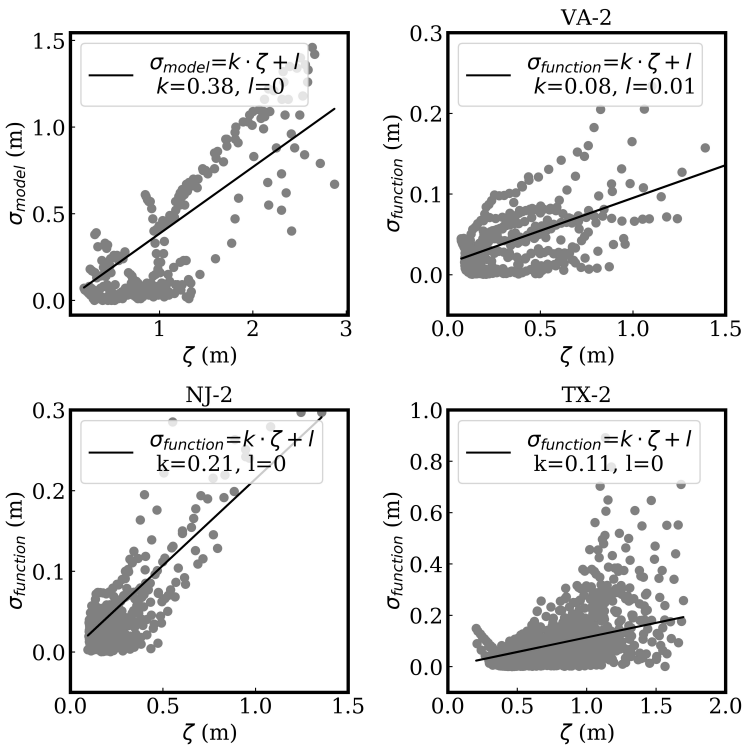

Figure 2.7: Surge magnitude prediction uncertainty quantification. σ_{model} is calculated as simulated surge standard deviation with respect to observations (NOAA, 2017) due to wind parameterization and hydrodynamic modeling based on ADCIRC-STWAVE and ADCIRC-SWAN simulations at selected coastal locations. Shown are US Atlantic Hurricanes Sandy (2012), Irene (2011), Isabel (2003), Gloria (1985), Josephine (1984) (Cialone et al., 2015) and US Gulf of Mexico Hurricanes Ike (2008), Katrina (2005), and Rita (2005) (Bunya et al., 2010a; Cialone et al., 2015), for surge 24 to 6 hours before landfall. $\sigma_{function}$ is calculated as error in surge prediction using Equations 2.2 and 2.3, represented by standard deviation between curve fit and surge simulations at VA-2 (Virginia Beach) NJ-2 (Sandy Hook), and TX-2 (Galveston), for surge 24 to 6 hours before landfall. Each gray dot represents surge values averaged over a 1-hour interval.

(Figure A6). Though Hurricane Harvey's (2017) recent landfall was 250 km to the south of Galveston Pier 21, we predict its forerunner surge 12 hours before landfall to be 0.4-0.9 m, while the observed value was 0.5 m (Figure A7). The arrival of a 0.5-m forerunner during Harvey is predicted to be 15 ± 7 hours before landfall, while the observed was 18 hours before landfall (Figure A7).

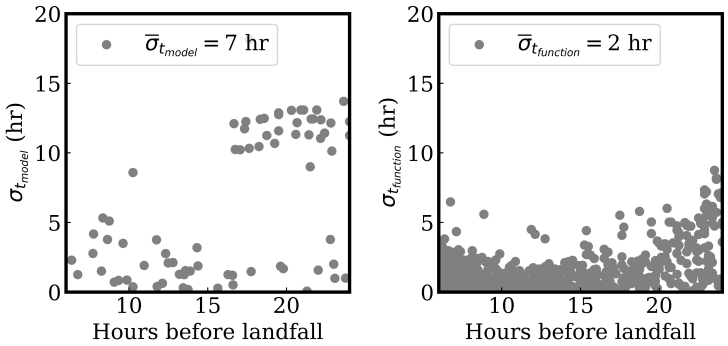

Figure 2.8: Surge timing prediction uncertainty quantification. (a) Simulated timing standard deviation (NOAA, 2017) due to wind parameterization and hydrodynamic modeling based on ADCIRC-STWAVE and ADCIRC-SWAN simulations at selected coastal locations. Shown are US Atlantic Hurricanes Sandy (2012), Irene (2011), Isabel (2003), Gloria (1985), Josephine (1984) (Cialone et al., 2015) and US Gulf of Mexico Hurricanes Ike (2008), Katrina (2005), and Rita (2005) (Bunya et al., 2010a; Cialone et al., 2015), for the arrival of 0.3-m to 2.0-m surge. (b) Error in timing prediction when observed forerunner surge is between 0.3-m to 2.0-m using Eqs. 2 and 3.

These prediction-observation comparisons demonstrate that Equations 2.2 to 2.4 captures the predominant physical mechanisms governing forerunner surge. The slight underestimation for forerunner surge during Hurricane Ike at 18 and 12 hours before landfall is expected, considering the employed hydrodynamic model underestimates surge for this event during this period. This prediction could be more accurate with future hydrodynamic model improvements. The overall uncertainty can be reduced with improved forecasting of the spatial wind field as well as with improved operational forecast storm surge models.

Finally, we conduct extreme value analyses using Equations 2.2 to 2.4 and existing joint probability statistics in Hampton Roads (Nadal-Caraballo et al., 2015), New York/ New Jersey, and Galveston (Niedoroda et al., 2010; Irish et al., 2011b). To estimate 1% annual exceedance probabilities (AEP) for forerunner surge, we employ the joint probability method with optimal sampling (JPM-OS; (Resio et al., 2009)) achieved using time-evolving surge response functions of Equations 2.2 and 2.3. The joint probability density function is

$f = f(R|\Delta p)f(\Delta p|x_o)f(v_f|x_o)f(x_o)$. We use published parameterized probability density functions for the U.S. Gulf of Mexico (Irish et al., 2011b; Niedoroda et al., 2010) and U.S. Atlantic (Nadal-Caraballo et al., 2015) coasts to define $f(R|\Delta p)$, $f(\Delta p|x_o)$, $f(v_f|x_o)$, and $f(x_o)$, based on best available historical track information (e.g., (Landsea and Franklin, 2013; Powell and Reinhold, 2007); A. Cox, Oceanweather, Inc. personal communications). Only landfalling storms are considered, and dependence on storm heading is neglected. We present uncertainty ranges based on our estimated total standard deviation (Equation 2.4). Results show that the 1% annual exceedance probability (AEP) forerunner surge 12 hours before landfall is 0.53 ± 0.21 m at Virginia Beach, 0.71 ± 0.31 m at New York/ New Jersey, and 1.37 ± 0.54 m at Galveston. This preliminary probabilistic hazard assessment demonstrates the Houston-Galveston area is more prone to high forerunner surge, compared with Hampton Roads and New York/ New Jersey, which is expected considering the much wider and shallower continental shelf, generally lower bottom friction from the muddy sediments along the Texas coast, and more frequent intense storms.

2.4 Summary and Conclusions

Forerunner surge in advance of TC landfall can leave people stranded, preventing evacuation and rescue, thus leading to greater loss of life. With projected global sea level rise and projected changes in storm climatology, forerunner surge is expected to play an even more critical role in coastal hazards. Thus, it is of great importance to understand what storm conditions have the potential to generate large forerunner surge, and to include prediction of forerunner surge in public forecasts.

Our results confirm Ekman setup is the leading mechanism driving forerunner surge genera-

tion in surge-prone regions characterized by broad, shallow terrain. We further quantitatively prove that slow-moving, large, intense storms have the most potential for generating dangerous forerunner surge, because such storms generate and sustain the strong alongshore currents needed to produce Ekman setup.

The physical scaling presented herein can be used to assess trends in forerunner surge as a function of real-time forecasted storm track parameters only, allows identification of the range of storm conditions in which a large forerunner surge is possible. The forecasting equations also have the potential to be incorporated into coastal flooding warning systems, and may be used to aid emergency managers and communities in evacuation planning and execution. Because the predictive equations herein are physically based, they are also of high value to regions worldwide influenced by TCs and surge threats, such as the Pacific coasts of southeast Asia, west and east Australia (Eliot and Pattiaratchi, 2010), and the Bay of Bengal. In developing regions that lack sophisticated computer modeling, the methods and findings can be applied directly to gauge data or limited simulation results to better characterize forerunner surge threat.

While the TC climatology community has studied and come to consensus that future TCs will be more intense under global warming (IPCC, 2014; Knutson et al., 2010), little attention has been given to the influence of global warming on TC size and forward speed. Yet, such investigations are in critical need given the significant influence of size and forward speed on forerunner surge. Future work to improve understanding and ability to predict forerunner surge should consider, for example, the influence of locally generated surge in coastal bays, tides, sea level rise, and vertical flow structure (e.g, multi-layer hydrodynamic simulation) on Ekman setup.

2.5 Acknowledgements

This material is based upon work supported by the National Science Foundation under Grant Nos. CMMI-1206271 and EAR-163009, and the Mid-Atlantic Coastal Storms Graduate Research Fellowship (Project No. R/71858M). The work used resources of the Advanced Research Computing at Virginia Tech. The authors wish to thank the USACE for providing surge simulation data, Oceanweather, Inc. for allowing use of their PBL Model, Drs. Casey Dietrich and Joannes Westerink for providing the ADCIRC mesh and model setup used in Texas, and Dr. Andrew Kennedy for providing his observational data from Hurricane Ike. The Texas simulation data can be obtained in the supplemental material and the NACCS data is publicly available online.

Chapter 3

Physical Drivers of Changes in Probabilistic Surge Hazard under Sea Level Rise

Yi Liu[1], Taylor G. Asher[2], Jennifer L. Irish[1]

[1]Department of Civil and Environmental Engineering, Virginia Tech, Blacksburg, VA, USA

[2]Department of Marines Sciences, University of North Carolina at Chapel Hill, NC, USA

Submitted to Earth's Future.

Abstract

Surge hazards induced by tropical cyclones have caused heavy economic losses and casualties for coastal communities worldwide. Under projected sea level rise (SLR), how the probabilistic surge hazard will change is unclear. Coastal planning and engineering usually adopts the "bathtub" method to evaluate the surge-SLR response, where the surge hazard with SLR is considered to be the exact summation of the two. However, this direct summation has been shown by previous studies to be unreliable. Studies on surge-SLR response either use a low-fidelity model setup or rely on individual storm's surge to represent the probabilistic surge hazard due to high computational burden. Herein we use high-fidelity numerical models in the Tampa area, West Florida, consider nearly 200 synthetic storms and four sea level rise scenarios, and investigate the surge-SLR response and its physical drivers. Compared to the direct summation of present-day surge and SLR amount, results show that the probabilistic surge with SLR can be 1.0 m larger, while different individual storm's surge with the same magnitude as this probabilistic value can be 1.5 m larger or 0.1 m smaller, indicating the importance of not relying on results from a limited number of surge events to assess the probabilistic surge hazard change to SLR. Investigation of the physical drivers show that topography and storm forward speed notably affect the surge-SLR response. When considering 1.3 m or larger SLR in the study area, complex topography, and large surge events, the effects of sea level rise on the probabilistic surge hazard are hard to predict and should be investigated more carefully.

3.1 Introduction

Tropical cyclone induced storm surge is a perpetual issue facing a growing number of people residing on the coast worldwide. In the past few decades, storm surge has caused countless casualties and heavy economic losses during major tropical cyclones such as Hurricanes Katrina (2005), Ike (2008), Sandy (2012), Irma (2017), and Typhoon Haiyan (2013). To build more resilient coastal communities, understanding the probabilistic surge hazard, i.e., the flood elevation exceeded annually with a prescribed probability, is of critical importance. Projected sea level rise (SLR) causes changes to coastal hydrodynamics and geomorphology among other factors, leading to different surge heights induced by the same tropical cyclones. For example, a coastal city with a 1% annual exceedance probability (AEP) surge value of 1 m today may experience a 1% AEP surge of 0.5 m or 1.5 m in the future with SLR. Understanding how the probabilistic surge hazards respond to SLR is essential for coastal planning and engineering.

Researchers have been using numerical models to investigate how the probabilistic surge hazard will respond to sea level rise. Lin et al. (2012) simulated 2000 synthetic storms and evaluated surge probabilities under different climate change scenarios. However, to enable the large number of simulations for a complete probability evaluation, Lin et al. (2012) had to use a low resolution mesh and neglected waves. Based on the sensitivity tests using this low-fidelity model setup, they assumed that surge values would not change with rising sea levels, and used a so-called "bathtub" method to consider the impacts of SLR, where the surge value with SLR is calculated as exactly the summation between surge value with no SLR and the SLR amount.

While the "bathtub" method has been widely used for coastal planning and engineering

because of its convenience, it can often be inaccurate, making constructions based on the "bathtub" assumption unreliable and potentially putting people's lives and properties at risk. For example, Smith et al. (2010) simulated six storms under three SLR scenarios (0.0 m, 0.5 m, 1.0 m) for Southeast Louisiana using high-fidelity surge and wave models, and concluded that surge from individual storm does change with SLR-the surge levels could be increased by as much as 1-3 m above the SLR amount in certain areas. Bilskie et al. (2014) used a similar model setup in the same area with additional consideration of land use/land cover change induced by SLR, and also found that surge response to SLR was dynamic and sensitive to these landscape changes. However, because the high-fidelity hydrodynamic models used in these studies are computationally expensive, most studies used a limited number of tropical cyclones intended to produce surge values at a prescribed AEP as illustrative examples.

In order to explore changes in probabilistic surge hazard under multiple SLR scenarios and the physical drivers behind these changes, we select and simulate nearly 200 synthetic storms for each of the four SLR scenarios considered in our study area of Tampa, FL and its surrounding communities, which are densely populated and are projected to experience severe relative SLR. Here, we define the probabilistic surge hazard to be the statistical flood elevation including storm surge, wave setup, and astronomical tides. We investigate the physical drivers of the surge hazard change due to SLR, and found that factors including topographic change and storm forward speed have significant impacts on the surge-SLR response variations.

3.2 Methods

3.2.1 Sea Level Rise Scenarios

Various studies have been conducted on historical SLR quantification and future SLR projections. Based on satellite altimeter and in situ data, Church and White (2006, 2011) observed a global SLR rate of 1.7 ± 0.31 mm/year in the last century. Based on different representative concentration pathways (RCP) scenarios, global mean SLR is projected to rise by 0.26 to 0.98 m by 2081-2100 (1986-2005 basis) with a 95% confidence interval (Church et al., 2013; IPCC, 2014). Kopp et al. (2014) projected an even higher SLR of 1.2 m with a 90 probability by the end of this century (2000 basis). With maximum possible ice sheet loss considered, global SLR could be as high as 2.0 m by 2100 (1992 basis) (Rahmstorf, 2007; Vermeer and Rahmstorf, 2009; Parris et al., 2012). More recently, DeConto and Pollard (2016) projected that global SLR could be more than 15 m by 2500 considering Antarctica contribution only.

Regional SLR projections also need to consider local factors that may counterbalance or exacerbate the global SLR trend. For example, the eastern North Pacific coast has not experienced much SLR since the 1980s because of impacts from local wind stress patterns and ocean circulation fluctuations (Bromirski et al., 2011). In contrast, relative sea levels along the coast of the Gulf of Mexico (especially the northwestern part) and the US Mid-Atlantic have been rising substantially due to land subsidence induced by glacio-isostatic adjustment, drainage, groundwater and oil withdrawal (González and Tornqvist, 2006; Mitrovica and Milne, 2002; Nicholls and Cazenave, 2010). Our study area Tampa, Florida, for example, is undergoing land subsidence because of groundwater withdrawal and sinkhole problems (Tihansky, 1999).

Table 3.1: Selected SLR scenarios compared to the most recent NOAA 2100 SLR projections at St. Petersburg, Florida (Sweet et al., 2017).

Selected SLR Scenario (m)	Position in NOAA Projections
0.65	2040 (Extreme) - 2070 (Intermediate)
1.30	2060 (Extreme) - 2080 (Int-High)
1.95	2080 (Extreme) - 2090 (High)

Considering the above global and regional projections and leveraging the existing storm simulations with 1.30 m SLR in Tampa, Florida by the Federal Emergency Management Agency (FEMA), four SLR scenarios are selected for this study: 0.00 m, 0.65 m, 1.30 m, and 1.95 m. We purposefully select uniform increments of sea level rise to facilitate investigation of the physical drivers of surge hazard change. This selection also predominantly covers the range of the most recent 2100 SLR projections (Table 3.1).

3.2.2 Numerical Model for Surge Simulation

The model setup implemented in this study is based on that used in flood insurance studies by FEMA. The two-dimensional depth-integrated hydrodynamic model ADCIRC (Luettich et al., 1992) tightly-coupled with the spectral wave model SWAN (Booij et al., 1996) are used to solve the two-dimensional depth integrated shallow water equations for flood simulation (Westerink et al., 2008; Bunya et al., 2010b; Dietrich et al., 2010):

$$\begin{cases} \dfrac{\partial \zeta}{\partial t} + \dfrac{\partial UH}{\partial x} + \dfrac{\partial VH}{\partial y} = 0 & \text{(3.1a)} \\ \dfrac{\partial UH}{\partial t} + \dfrac{\partial UUH}{\partial x} + \dfrac{\partial UVH}{\partial y} - fVH = -H\dfrac{\partial}{\partial x}\left[\dfrac{p_s}{\rho_0} + g(\zeta - \alpha\eta)\right] + M_x + D_x \\ \qquad\qquad +B_x + \dfrac{\tau_{sx,wind}}{\rho_0} + \dfrac{\tau_{sx,wave}}{\rho_0} - \dfrac{\tau_{bx}}{\rho_0} & \text{(3.1b)} \\ \dfrac{\partial VH}{\partial t} + \dfrac{\partial VUH}{\partial x} + \dfrac{\partial VVH}{\partial y} + fUH = -H\dfrac{\partial}{\partial y}\left[\dfrac{p_s}{\rho_0} + g(\zeta - \alpha\eta)\right] + M_y + D_y \\ \qquad\qquad +B_y + \dfrac{\tau_{sy,wind}}{\rho_0} + \dfrac{\tau_{sy,wave}}{\rho_0} - \dfrac{\tau_{by}}{\rho_0} & \text{(3.1c)} \end{cases}$$

where ζ is the free surface elevation, U and V are depth-averaged horizontal velocities, H is total water depth, M is diffusion term, D is dispersion term, B is baroclinic forcing term, $\tau_{s,wind}$ is wind stress, $\tau_{s,wave}$ is wave stress, τ_b is bottom stress, η is tidal potential, α is Earth elasticity factor, ρ_0 is reference water density, and p_s is atmospheric pressure.

Both models share the same mesh, with ADCIRC passing water elevation and velocity information to SWAN while SWAN supplies the wave radiation stress fields to ADCIRC, so that the output water elevation includes wave setup. To include tides in the water level results, each tropical storm simulation is started at a random tidal phase, where the mean tide range is 0.48 m (NOAA, 2017). The meteorological wind and pressure fields driving ADCIRC+SWAN are developed with a planetary boundary layer (PBL) model (Thompson and Cardone, 1996) using storm track information.

Sea surface level in the ADCIRC+SWAN simulation is elevated by the amount of SLR for each scenario, and previously dry nodes that are now within the still-water contour line and connected to open water become wet at the start of the simulation. Following methods implemented in Irish et al. (2014) and Atkinson et al. (2013), a similar approach is taken to change bottom friction and surface roughness in response to land cover change induced by SLR. Morphological change induced by sea level rise is not considered.

3.2.3 Probabilistic Surge Hazard Assessment

Because of a limited observational record of storm surge data, it is important not to rely only on historical tropical cyclones to calculate storm surge frequencies (Irish et al., 2011a; Resio and Irish, 2015). Consequently, The Joint Probability Method (JPM) (Ho and Myers, 1975) has been adopted as the preferred method by US federal agencies to develop probabilistic

surge hazard assessment. The essence of the JPM is to consider all possible storms consistent with the local climatology, and the rate of occurrence of each storm is calculated by the product of the probability of each primary storm parameter, usually including pressure deficit (Δ_p), pressure scale radius (R_p), forward speed (v_f), heading (θ), and landfall location (x). Thus the continuous surge non-exceedance probability can be written as:

$$P(\eta) = 1 - \int_{\Delta p} \int_{R_p} \int_{v_f} \int_{\theta} \int_{x} \Lambda_{\Delta p} \Lambda_{R_p} \Lambda_{v_f} \Lambda_{\theta} \Lambda_{(\lambda,x)} P(\epsilon) H[\eta - \Psi(\Delta_p, R_p, v_f, \theta, x) + \epsilon] dx d\theta dv_f dR_p d\Delta p d\epsilon \tag{3.2}$$

where η is the surge magnitude at a fixed spatial location, Λ_i is the probability density of an individual parameter, $\Lambda_{(\lambda,x)}$ is the storm rate per unit coastline, $\psi(c_p, R_p, v_f, \theta, x)$ is estimated surge given a specific storm condition, and $H[\cdot]$ is the Heaviside function. The uncertainty term ϵ captures wind and surge simulation deficiencies and is included in the integral following method in Resio et al. (2009, 2013).

Storm selection for surge simulation

One major shortcoming of the traditional JPM is that when combined with the high-resolution hydrodynamic and wave models used today, simulation of the large number of storms needed to rationally evaluate surges (i.e., Ψ in Equation 3.2) associated with the continuum of the JPM probabilities is not possible given the computational demands of these models. Optimal Sampling (OS) approaches are thus used to decrease the number of storm simulations needed while minimizing loss of accuracy in the surge hazard calculation. Here we make use of the Tampa FEMA study's storm set, where a Bayesian Quadrature (BQ) integration scheme is used. In BQ, probability masses for each storm scenario are assigned so that the integration of a limited number of representative storms can be used to approx-

imate the JPM integration with reasonable accuracy (Toro et al., 2010a,b). The resulting optimal storm set for the Tampa FEMA study is 664 unique synthetic storms, in order to characterize AEPs ranging from 10% to 0.2% over a larger geographic than is used in this study.

Further reduction of the storm set was performed to eliminate unneeded storms and limit the computational burden. This was done by evaluating the contribution of each storm to the 1% AEP with the already-completed 664 simulations at current sea level. Storms that exceed a threshold are retained. Using this method, we are able to capture a large portion of the surge probability using a subset of 188 out of 664 JPM-OS-BQ storms. Comparing the probabilistic surges in the study area for present-day sea level using the subset of 188 storms and the full set of 664 storms, the difference is well within 0.03 m for 1% AEP, and within 0.05 m for 2% and 0.2% AEP. Probabilistic surge hazard maps with an AEP of 2%, 1%, and 0.2% for each of the four SLR scenarios (a total of 752 simulations) are generated using these 188 storms.

3.2.4 Analysis Methods

To investigate the surge-SLR response, specifically the change of the surge hazard due to SLR, a dimensional nonlinearity (DNL) index is introduced:

$$DNL = \eta_{SLR} - (\eta_0 + SLR) \tag{3.3}$$

where η_{SLR} and η_0 are water elevations, relative to present-day mean sea level, generated under a specific SLR scenario (λ_0 means no SLR), and SLR is the magnitude of the sea level rise. Based on this definition, a negative DNL represents a sublinear surge-SLR response

where the increase of the probabilistic surge value is less than the SLR magnitude, and a positive DNL shows the presence of a superlinear surge-SLR response where the surge increases more than the SLR magnitude. Where response is perfectly linear, the index DNL is 0. This surge-SLR nonlinearity is closely examined for surge generated by a single storm and the probabilistic surge at prescribed AEP.

One question of interest is how the relative influence of different storm parameters changes under SLR. To this end, we introduce the following method to evaluate the probability-contribution-weighted mean value of a storm parameter, corresponding to a given sea level and AEP:

$$\hat{X}_{(SLR,\eta)} = \frac{1}{N}\sum_{i=1}^{N} X_i P(\eta) \tag{3.4}$$

where X is the value of a given storm parameter, i is an index for each storm, N is the total number of storms, $P(\eta)$ is the JPM integral (Equation 3.2) for the selected AEP surge η, and the hat over X denotes the probability-contribution-weighted mean. Because this calculation implicitly takes into account the value of the storm parameter, its likelihood, and the resulting surge, it is a useful method to infer what values tend to dominate the surge response at the selected AEP.

3.3 Results

The 1% AEP surge hazard maps generated using results from the 188 selected storms under the four SLR scenarios (0.00, 0.65 m, 1.30 m, and 1.95 m) are shown in Figure 3.2 (Figure S3 and S4 show 2% and 0.2% AEP surge hazard). Comparing the four maps shows how, as expected, the inundation area increases as SLR increases. From these maps, it can be seen that the surge hazard magnitude is amplified in the Sarasota Bay region, with respect to

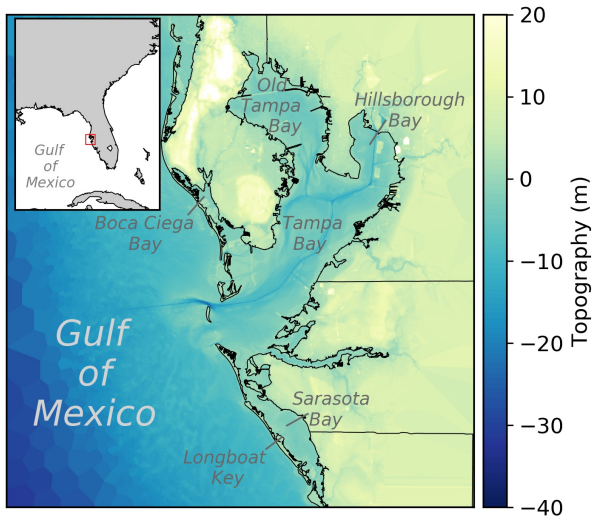

Figure 3.1: Study area showing topographic contours.

other locations. Figure 3.3 shows the DNL index maps for the 0.65 m, 1.30 m, and 1.95 m SLR scenarios for 1% AEP surge hazard. The DNL maps clearly show a general sublinearity in most of the study area, especially on the open coast and on the northeast side of Tampa Bay. The exception is the aforementioned superlinearity in Sarasoa Bay, especially for the 1.30 m and 1.95 m SLR scenarios. Normalizing these nonlinearities show that in Sarasota Bay, the superlinearity can be almost 40% of the SLR amount, or 25% of the present-day 1% AEP surge (Figure 3.4)

To investigate how nonlinearities vary with SLR magnitude, Figure 3.5 shows the probabilistic surge value change ($\eta_{SLR} - \eta_0$) versus SLR scenario (λ) at five representative locations. The deviation from the 1:1 slope line is the nonlinearity represented by the DNL, where a point falling on the reference line with a slope 1:1 means that the probabilistic surge value change equals the SLR value, representing a perfectly linear response (DNL=0). These plots show that very few points fall on the 1:1 reference line, providing further evidence that some

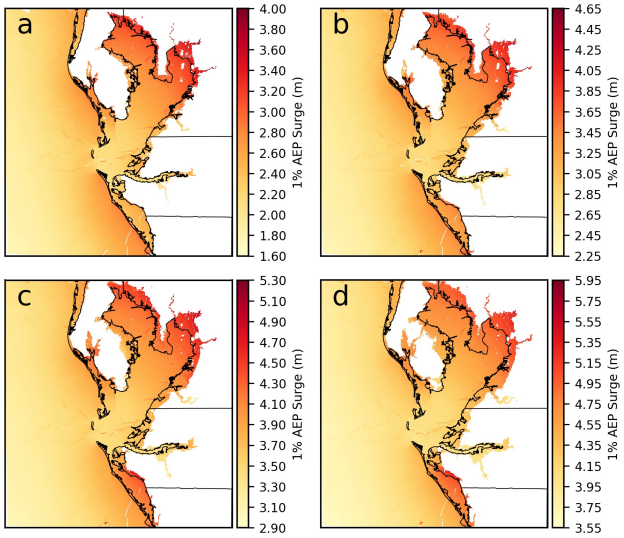

Figure 3.2: 1% AEP probabilistic surge hazard maps calculated from 188 tropical cyclones under four SLR scenarios: a) present-day, b) 0.65 m, c) 1.30 m, and d) 1.95 m. The color bars are selected so that the same color in each map represents a perfectly linear surge-SLR response, i.e., the probabilistic surge with SLR will be the exact summation of the two.

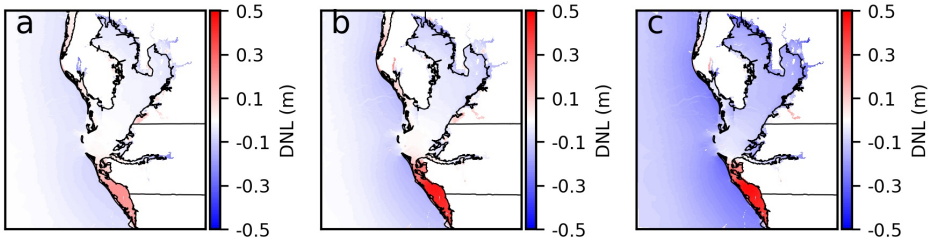

Figure 3.3: Dimensional Nonlinearity ($DNL = \eta_{SLR} - \eta_0 - \lambda$) index maps for the 1% AEP surge when considering three SLR scenarios: a) 0.65 m, b) 1.30 m, and c) 1.95 m.

degree of surge-SLR nonlinearity exists for all of the SLR scenarios. The trend with SLR for any given AEP indicates varying degrees of nonlinearity. For example, location a in front of Longboat Key experiences a nearly linear increase in sublinearity as SLR increases, while the superlinearity at location b within Sarasota Bay increases linearly with SLR for SLR less than 1.30 m, but stays constant for SLR larger than 1.30 m. At both locations a and b, the more extreme surges (i.e., smaller AEP) experience larger nonlinearity. For locations c and e, different AEP surge values show similar trend, where location e exhibits negligible

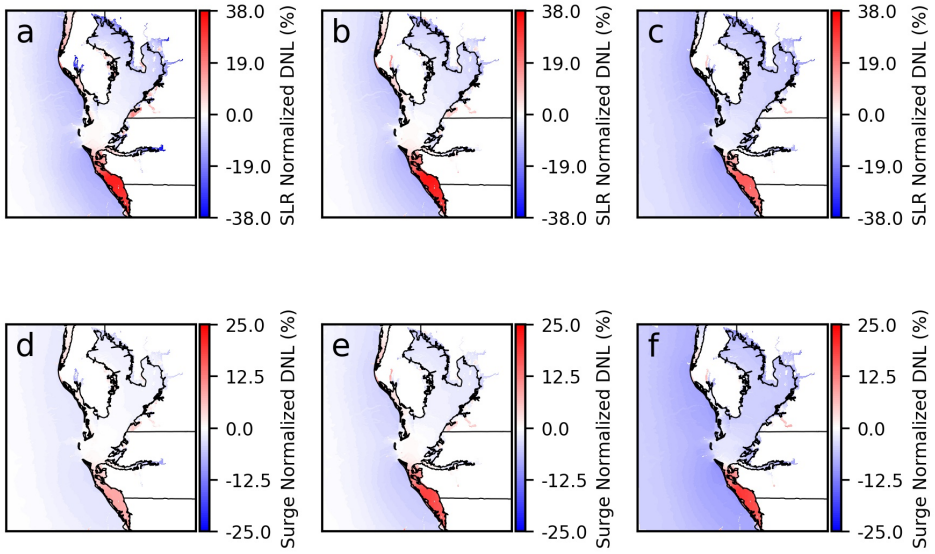

Figure 3.4: SLR normalized DNL maps (first row) and present-day surge normalized DNL maps (second row) for the 1% AEP surge when considering three SLR scenarios: a) & d) 0.65 m, b) & e) 1.30 m, c) & f) 1.95 m.

nonlinearity. The situation is more complicated at location d: for surge values with an AEP less than 1%, the sublinearity increases drastically as SLR increases to 0.65 m and then the DNL drops to almost zero. For 0.2% AEP surge at location d, the DNL is zero until SLR is more than 0.65 m, at which point a superlinearity is introduced. This superlinearity increases from 0.65 m to 1.30 m and stays constant from 1.30 m to 1.95 m SLR.

Another way to explore nonlinearity is to examine and compare how the nonlinearity changes for both individual storms and for probabilistic surges. The two locations a and b around Sarasota Bay (see Figure 3.5) are selected to show the variations in nonlinearity. As shown in Figure 3.6, the trend in nonlinearity among individual storm surges generally matches that of the probabilistic surges in most instances. However, there is appreciably more scatter in individual storms' nonlinearity. Even for very large individual surge events, some storms exhibit no nonlinearity or a nonlinearity in the opposite direction of the general trend at the location. At the bay location b, there are a number of individual storms whose surge exceeds

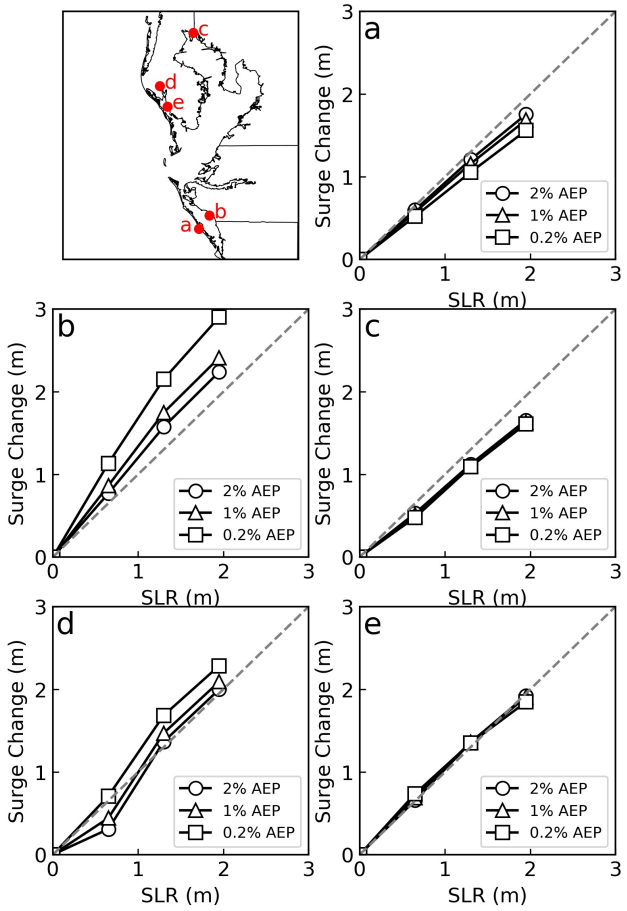

Figure 3.5: Probabilistic surge change vs SLR plots at selected locations.

3 m and that exhibit significantly lower DNL. This finding emphasizes the importance of considering a wide range of synthetic storms when projecting future probabilistic surge under SLR.

The degree of nonlinearity in the probabilistic surges also tend to be smaller (i.e., closer to zero) than that of the individual storm surges. This is most likely related to the fact that probabilistic surges are driven most by surges slightly smaller than the probabilistic surge magnitude (a byproduct of the uncertainty).

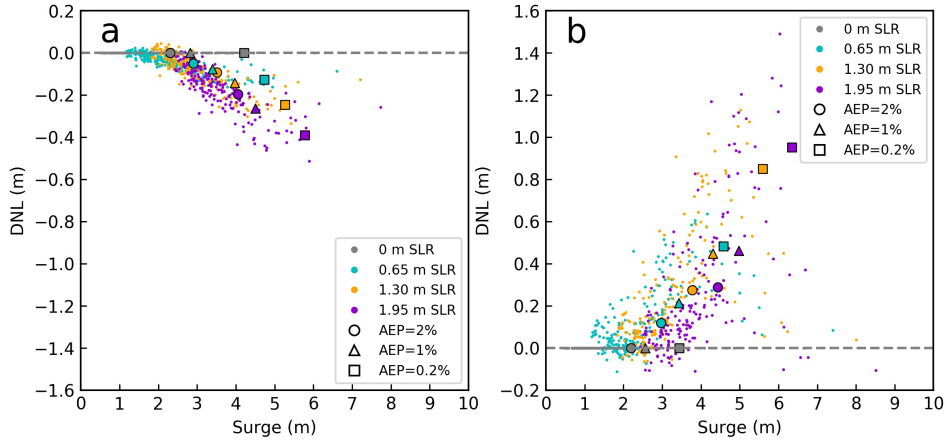

Figure 3.6: Surge nonlinearity (represented by DNL) at locations a and b around Sarasota Bay. The dashed gray lines represents no nonlinearity. Different color represents different SLR scenario; different symbols represent different AEP.

3.4 Discussion

In order to understand why surge-SLR nonlinearities arise, we investigate several potential physical drivers of these nonlinearities. We found the influence of the region's topography and the influence of storm forward speed are the primary drivers of nonlinear surge-SLR response. While studies (e.g., (Woodruff et al., 2013; Bilskie et al., 2014)) have shown that long-term coastal evolution under SLR will have an impact on future probabilistic surge hazard, direct consideration of this complex phenomenon is out of the scope of this study. The argument for this assumption is that the area is highly developed and much of the shoreline behind the open coast is hardened. Along the open coast, the beaches are heavily managed and frequently nourished, complicating any approach to modeling long-term evolution. Nevertheless, the impact of long-term coastal evolution is included in the supplemental material as a sensitivity test (Text S1 and Figure S1-S2).

3.4.1 Topographic Drivers of Surge-SLR Nonlinearity

SLR introduces changes to surge hydrodynamics in various ways depending on local topography. First of all, increased water levels decrease bottom friction in general, leading to an overall sublinearity in most of the study area. Other factors including redirected flow path and increased inundation extent can cause either superlinearity or sublinearity depending on specific interactions between increased water levels and local topographic features.

For example, the notable superlinearity in Sarasota Bay is believed to result from more overtopping on Longboat Key in front of Sarasota Bay as sea levels rise. Because the average elevation of Longboat Key is around 1.30 m above present-day mean sea level and that Sarasota Bay's opening is small, with SLR more storms can produce surges that overtop this barrier island, especially at the 1.30-m scenario. When overtopping occures, the surge level varies smoothly from the open coast to Sarasota Bay, indicating a failure of Longboat Key's surge blocking function (Figure 3.7). This also explains why the superlinearity increases when SLR is less than 1.30 m but stays constant when SLR is larger than 1.30 m (Figure 3.5). For comparison, Boca Ciega Bay in the north has a relatively lower barrier island and wider opening, thus less surge-SLR nonlinearity is induced.

Although the increased overtopping of Longboat Key as sea level rises greatly contributes to the superlinearity in Sarasota Bay, the degree to which the inundation extent increases with SLR is also a factor for the 1.30-m and 1.95-m SLR scenarios. The influence of floodplain extent on surge hazard nonlinearity is demonstrated by comparing surge hazard maps behind the inner coastlines of Old Tampa Bay and Sarasota Bay under different the SLR scenarios (Figure 3.7). From the figure of Old Tampa Bay, it is clear that SLR enables flooding farther inland under the two more extreme SLR scenarios. The inundation area of the 1%

AEP floodplain extends farther inland for an average distance of more than 2.5 kilometers (km) in northern Old Tampa Bay, while inundation area extends nearly 1 km farther in northeast Sarasota Bay. Though SLR facilitates the flow of water farther inland, elevated ground and the correspondingly increased bottom friction restrict the motion of water. While bottom friction generally increases with ground elevation in both northern Old Tampa Bay and northeast Sarasota Bay in a similar fashion, the topographic gradient is different in these two places. The former has a wide low-lying region near the coastline, while the latter is characterized by a more steeply sloping terrain. The more abrupt and extensive increase in inundation extent in Old Tampa Bay helps to shape the overall sublinearity there. In Sarasota Bay, the combination of more water entering the bay by overtopping and a more steeply sloping terrain act to enhance superlinearity.

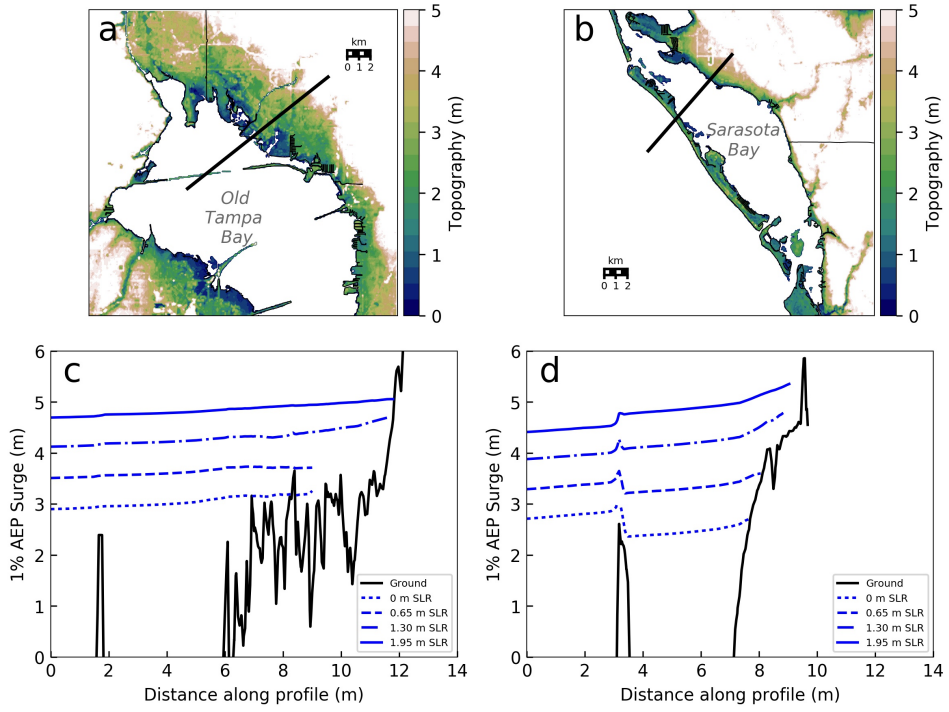

Figure 3.7: Transects of 1% AEP surges at Old Tampa Bay (a & c) and Sarasota Bay (b & d) for all SLR scenarios.

3.4.2 Storm Drivers of Surge-SLR Nonlinearity

The influence of storm parameters, including central pressure deficit, size, forward speed, and heading, on surge development can potentially change with increasing sea level. Using Equation 3.4, results show that the range of intensity, size, and heading influencing a specified AEP value remains largely unchanged as sea level rises (Figure S6-S8). However, the range of forward speed influencing a specified AEP value does vary with SLR in some places (Figure 3.8). At the inner coastlines of Sarasota Bay and Boca Ciega Bay, the mean value of forward speed (V_f) shifts from around 8.5 m/s under present sea level to around 10 m/s as sea level increases by 1.95 m, meaning as sea level increases, faster-moving storms become more important and contribute more to the probabilistic surges at the inner coastlines of these bays. The opposite is seen at the open coast. This indicates that the forward speed drives nonlinearity for the probabilistic surge.

In addition to influencing the duration a storm remains in the region, the forward speed of a tropical cyclone has the effect of deforming the wind field. Although the interaction between translation and rotation of a storm (along with Coriolis forcing) is very complicated, the effect of forward speed on the wind field can be thought of as roughly the vector sum of the two (Thompson and Cardone, 1996). Namely, a faster-moving storm strengthens winds on the forward right side of the storm, in the Northern Hemisphere, where the highest winds and peak storm surge typically are seen. This means that forward speed can both elevate (due to high winds) and dampen (due to shorter duration) storm surge response, depending on the specific storm, setting and location of interest. This explains why in the study area the contribution-weighted mean V_f is highest along the open coast, but decreases behind barrier islands and in Tampa Bay, and also why the contribution-weighted mean V_f increases behind the barrier islands for higher SLR scenarios. In this case, fast-moving storms (V_f of around

10 m/s) dominate the probabilistic surge hazard at the open coast because their higher wind speeds lead to higher surges. In Sarasota Bay, and to a lesser extent in Boca Ciega Bay, the mean contribution is somewhat slower (V_f of about 8 to 9 m/s). This is because the slower-moving storms can move more water from the ocean into the bays since they last longer, whereas faster storms' surge magnitudes are limited by the duration of the event.

With increasing SLR, the barrier islands become less of a barrier to flow, such that they are no longer as effective in sheltering the mainland coast from direct ocean surge exposure. This loss of protection gives rise to strong superlinearity associated with fast-moving storms. In turn, as sea level rises, these fast-moving storms contribute more and more to the 0.5% to 2% AEP probabilistic surge levels along the mainland coast of Sarasota Bay. At the same time, the slower storms with weaker, longer-duration winds and correspondingly weaker superlinearity become less relevant to the probabilistic surge hazard in this area.

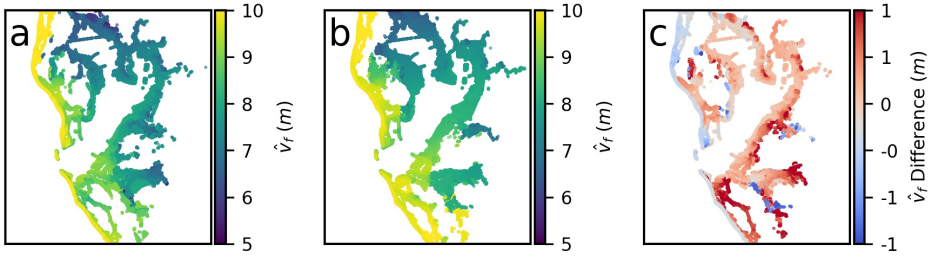

Figure 3.8: 1% AEP Contribution-weighted mean value of forward speed ($\hat{v}_{f(SLR,\eta)} = \frac{1}{N}\sum_{i=1}^{N} v_{f_i} P(\eta)$ based on Equation 3.4) at all locations of interest in the study area for a) present-day, b) 1.95 m SLR scenario, and c) the difference between the two.

3.5 Conclusions

The results herein show some degree of surge-SLR nonlinearity exists for most of the SLR scenarios in the study area. However, at least under the lower SLR scenarios, the nonlinearity

is small in most areas. It is less than one twentieth of the 1% AEP surge outside of Sarasota Bay and northern Old Tampa Bay under the 0.65 and 1.30 m SLR scenarios, but exceeds 10% in much of the study area at the high 1.95 m SLR scenario. This means that adding SLR to the probabilistic surges linearly, i.e., using a "bathtub" approach where the world coastlines are assumed to form a giant bathtub and no surge-SLR nonlinear response will occur, may still be informative under lower SLR scenarios, but in this study area loses significant accuracy when SLR is above 1.30 m .

It should be pointed out that the biggest nonlinearities come from topographic influences. Specifically, with SLR, the major flow obstructions such as barrier islands and elevated roadways lose their effectiveness (e.g., Longboat Key), and newly permanently wetted low-lying ground provides more space for water to flow (e.g., northeastern Old Tampa Bay). In reality, the nonlinearity can be even larger since SLR will erode dunes on barrier islands. While a sensitivity test of degraded dunes is included in the supplemental material, future work should further consider the impacts of SLR-induced topographic change. These topographic influences are not immediately apparent from the governing equations since they are not readily manifested as forcing terms. However, they stand out as the greatest drivers of nonlinearity in all parts of the study area. When investigating the response of probabilistic surge hazard to SLR, anywhere that the statistical floodplain is close to a major topographical feature, such as a barrier island or extensive flat ground, nonlinearity is expected to be larger. Thus, instead of relying on the simple "bathtub" approach, dynamically simulating SLR effects at these places becomes important for accurate projection of the future probabilistic surge hazard.

The range of individual surge-SLR nonlinearity grows with surge magnitude; i.e., the larger the surge value is, the more difficult it is to predict the response of this surge event to SLR.

This makes extreme storm events under SLR scenarios unpredictable and it can be very dangerous to rely on the surge-SLR response of one storm event to estimate the response of another storm event.

For all SLR scenarios tested, largest superlinearity in probabilistic surge is observed in Sarasota Bay, and notable sublinearity is seen along the open coast and within Old Tampa Bay. These nonlinearities are caused by complex interactions between different mechanisms, including but not limited to change in floodplain extent and contributions of storm parameters to the probabilistic surge hazard. First, a large increase in the inland extent of inundation induces sublinearity. Second, surges from fast storms are usually more sensitive to SLR, especially in areas close to the first and secondary coastlines.

Several assumptions made through the study render its limitations. It is assumed that no change will occur in coastal morphology, and there will be no anthropogenic response (e.g., flood control structures) to SLR. In reality, increased sea levels can degrade dunes and barrier islands, and new developments and mitigation measures will be introduced to the study area, all of which introduce further uncertainty in the surge-SLR response.

Nevertheless, the results presented herein have important implications for surge-SLR response studies. All in all, when considering low SLR scenarios and small surge events in regions where no obvious watercourse change under SLR, the "bathtub" method of assuming no nonlinearity with surge-SLR response may be useful. On the contrary, when considering higher SLR, large surge events, and/or regions with obvious watercourse change under SLR (e.g., failure of flow obstructions, wider flow openings, and limited drainage paths), surge is expected to respond more nonlinearly and less predictably to SLR. In these cases, the influence of surge-SLR nonlinearities should be examined more closely to guide future planning, engineering, and mitigation measures, ensuring more robust coastal development and more

resilient coastal communities.

Acknowledgements

The authors wish to thank The Edna Bailey Sussman Fund for funding and AECOM for facilitating this study. We also thank the Federal Emergency Management Agency for providing the ADCIRC mesh and other data, and Oceanweather Inc for providing the meteorological data. This material is based upon work supported by the National Science Foundation under Grant Nos. CMMI-1206271 and EAR-1630099. This work used resources of Advanced Research Computing at Virginia Tech and resources of WorldWinds, Inc..

Chapter 4

Impact of Sea Level Rise on the Temporal Evolution of Storm Surge

Yi Liu[1], Jennifer L. Irish[1]

[1]Department of Civil and Environmental Engineering, Virginia Tech, Blacksburg, VA, USA

In Preparation.

Abstract

Tropical cyclones and induced storm surges have been the leading causes of damage by natural hazards to coastal communities. While the majority of the surge induced damage is associated with peak surge, the temporal evolution of surge is important for evacuation and erosion problems. How the temporal evolution of surge respond to sea level rise is understudied. Herein, seven synthetic storms are simulated in the Tampa Bay region, West Florida, with four sea level rise scenarios considered. Surge anomaly time series and inundation extent are examined to investigate how sea level rise will impact them. Results show that peak surge can arrive 2-3 earlier in Sarasota Bay and 6 hours later in Old Tampa Bay with sea level rise. Surge more rapidly increase prior to peak at the north opening of Sarasota Bay, and the whole surge evolution profile shifts about 3 hours earlier in time at the south opening. Surge induced inundation extent increases nonlinearly with sea level rise and can be 1 km wider than expected in Sarasota Bay for the slow storm. Lastly, storm surge induced inundation area changes with sea level rise, and is the maximum in the present-day situation in the study area. Future coastal planning and engineering should thus not only take into account the impact of sea level rise on peak surge and probabilistic surge, but also the impact of sea level rise on the temporal evolution of storm surge.

4.1 Introduction

Over the last decades, tropical cyclones and induced storm surges have been the leading causes of damage by natural hazards to coastal communities. With more and more people moving to the coast and with projected sea level rise, understanding how surge hazards will change and how to protect people from these natural disasters is of great importance.

While the landfall of a tropical cyclone usually brings the maximum surge to the open coast, associated with the majority of the total damage, surge hazard is much less studied as a temporal process. Forerunner surge, an early water level elevation before a tropical cyclone landfall, has been thought to be small and insignificant (Bunpapong et al., 1985) until Hurricane Ike (2008), when a 1-2 m forerunner surge was generated approximately 12 hours before Ike's landfall, stranding many people on Galveston Island, increasing property losses and people's suffering (Kennedy et al., 2011). More recently, Sebastian et al. (2014) studied surge time series from different synthetic storms modified from Hurricane Ike's wind field in Galveston Bay. Jia et al. (2016) developed a surrogate model for surge time series prediction along the Louisiana coastlines.

According to the most recent studies (IPCC, 2014; Sweet et al., 2017), sea level has been rising at a global rate of 1.7 ± 0.31 mm/year in the last century, and is projected to continue rising by 0.26 to 0.98 m by 2081-2100 (1986-2005 basis) with a 95% confidence interval. This increasing sea level changes the initial water level along the coast, changing the hydrodynamics, thus the spatiotemporal evolution of storm surge. Many studies show that sea level rise will have an impact on peak surge. For example, Smith et al. (2010) and (Bilskie et al., 2014) used hydrodynamic models to simulate the dynamic effects of sea level rise on peak surge, and found that peak surge with sea level rise can be 3 m larger than the summation of present-

day surge and sea level rise amount at certain places in Louisiana. Yet, little to no existing literatures investigates the impacts of sea level rise on the temporal evolution of storm surge.

Increased water depth and permanent inundation associated with sea level rise can result in several changes in the storm-induced surge develop and propagating profiles. Understanding these changes help communities to better prepare for surge hazards in the future. For example, one of the influencing factors on the temporal evolution of storm surge is the continental shelf wave or Ekman setup, which is produced in a continental shelf area where there is a sea-bed slope and a geostrophic balance between along-shelf velocities and surface elevations (Pedlosky, 1990). Continental shelf waves are also believed to be the main contributor to Hurricane Ike's large forerunner surge (Kennedy et al., 2011). In the northern hemisphere, these waves travel such that the coastline is always on their right side. During tropical cyclones, continental shelf waves can be generated when the wind field is largely parallel to the shoreline, which drives alongshore currents, and where there is a relatively shallow, wide continental shelf for the waves to develop. On the west coast of Florida, shelf waves have been observed most notably during Hurricane Dennis (Morey et al., 2006) and a historical unnamed storm that generated a shelf wave resulting in a sea surface elevation as high as 1.5 m in Tampa Bay (Cline, 1920). With SLR imposed, water depth increases in the shelf area, which can result in a smaller and faster-moving shelf wave, contributing to a different surge time series evolution, causing nonlinearities in surge maxima, as well as in forerunner surge before a tropical cyclone landfall.

Herein we use high-fidelity models to study how sea level rise impact the temporal evolution of storm surge in the Tampa Bay region of West Florida. Results show that the forerunner surge and peak surge can respond very differently to sea level rise in the study area.

4.2 Methods

We use the high-fidelity hydrodynamic model ADCIRC (Luettich et al., 1992), coupled with a spectral wave model SWAN (Booij et al., 1996) (Bunya et al., 2010b; Dietrich et al., 2010). ADCIRC is a finite element model solving the two-dimensional depth integrated shallow water equation for flow velocity and water elevation:

$$\frac{\partial \zeta}{\partial t} + \frac{\partial UH}{\partial x} + \frac{\partial VH}{\partial y} = 0 \tag{4.1}$$

$$\frac{\partial U}{\partial t} + \frac{\partial UU}{\partial x} + \frac{\partial UV}{\partial y} - fV = -\frac{\partial}{\partial x}\left[\frac{p_s}{\rho_0} + g(\zeta - \alpha\eta)\right] + \frac{1}{H}(M_x + D_x + B_x + \frac{\tau_{sx,wind}}{\rho_0} + \frac{\tau_{sx,wave}}{\rho_0} - \frac{\tau_{bx}}{\rho_0}) \tag{4.2}$$

$$\frac{\partial V}{\partial t} + \frac{\partial VU}{\partial x} + \frac{\partial VV}{\partial y} + fU = -\frac{\partial}{\partial y}\left[\frac{p_s}{\rho_0} + g(\zeta - \alpha\eta)\right] + \frac{1}{H}(M_y + D_y + B_y + \frac{\tau_{sy,wind}}{\rho_0} + \frac{\tau_{sy,wave}}{\rho_0} - \frac{\tau_{by}}{\rho_0}) \tag{4.3}$$

where ζ is the free surface elevation, H is total water depth, U and V are depth-averaged horizontal velocities, M and D are diffusion and dispersion terms respectively, B is baroclinic forcing term, $\tau_{s,wind}$ and $\tau_{s,wave}$ are wind and wave stress terms, τ_b is bottom stress, η is tidal potential, α is Earth elasticity factor, ρ_0 is reference water density, and p_s is atmospheric pressure. Among the forcing terms, the wave stress information ($\tau_{s,wave}$) is passed from SWAN, the spectral wave model, so that ADCIRC's calculated water elevation (ζ) includes wave setup.

The input meteorological forcing is generated using the Planetary Boundary Layer (PBL) model (Thompson and Cardone, 1996), which calculates a hurricane's wind and pressure fields using storm track parameters, such as pressure deficit Δp, pressure scale radius R_p, forward speed v_f, heading (θ) and storm position x. Based on one synthetic storm making

landfall in the study area (storm 1 in table 4.1, Figure 4.1), storm track parameters including pressure deficit Δp, pressure scale radius R_p and forward speed v_f are varied to cover the possible range of the storm climatology in this area according to the Tampa FEMA study. Seven storms along the same track are simulated in total (Table 4.1), where storm 1 is the reference storm, storm 2&3 have increasing pressure deficit Δp, storm 4&5 have increasing pressure scale radius R_p, and storm 6&7 have decreasing forward speed v_f.

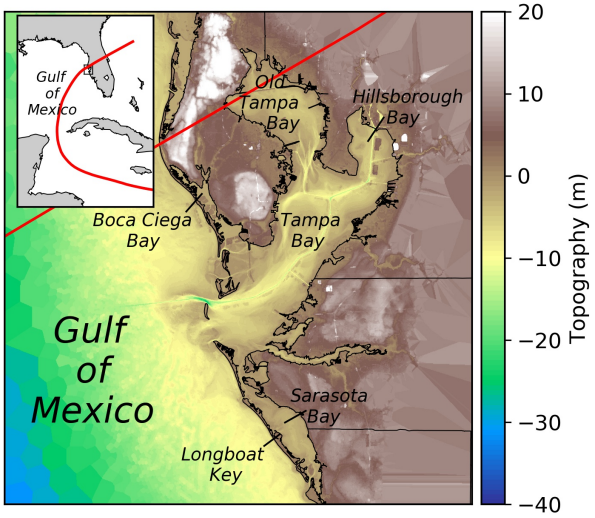

Figure 4.1: Topographic map of the study area. Red line represents the storm track

To examine the impacts of sea level rise on the temporal evolution of storm surge, four sea level rise scenarios are selected: present-day (no sea level rise), 0.65 m, 1.30 m, and 1.95 m. These scenarios increase with uniform increments and predominantly cover the most recent NOAA 2100 sea level rise projections at St. Petersburg, Florida (Sweet et al., 2017). For example, the 0.65 m sea level rise is projected to happen between 2040 (Extreme) and 2070 (Intermediate), and the 1.95 m sea level rise scenario is projected to happen between 2080 (Extreme) and 2090 (High).

To investigate the impacts of sea level rise on the temporal evolution of storm surge, a dimensional nonlinearity (DNL) index is introduced:

$$DNL(x,t) = \eta_{SLR}(x,t) - [\eta_0(x,t) + SLR] \tag{4.4}$$

where $\eta_{SLR}(x,t)$ and $\eta_0(x,t)$ are water elevations at geographic location x at time t, relative to present-day mean sea level, generated under a specific sea level rise scenario (λ_0 means no sea level rise), and SLR is the magnitude of the sea level rise. Based on this definition, a negative DNL represents a sublinear sea level rise impact where the increase of the surge magnitude is less than the sea level rise magnitude, and a positive DNL shows the presence of a superlinear sea level rise impact where the surge increases more than the sea level rise magnitude. Where response is perfectly linear, the index DNL is 0. Wherever and whenever DNL is not equal to 0, sea level rise has a nonlinear impact on the temporal evolution of storm surge. This nonlinearity is examined for surge generated by the aforementioned storms and sea level rise scenarios.

Table 4.1: Track parameters of the simulated storms in the study area.

Storm Name	$\Delta p(hPa)$	$R_p(km)$	$v_f(knots)$
storm 1	46.04	21.6	23.85
storm 2	*76.04*	21.6	23.85
storm 3	*106.04*	21.6	23.85
storm 4	46.04	*61.6*	23.85
storm 5	46.04	*101.6*	23.85
storm 6	46.04	21.6	*14.85*
storm 7	46.04	21.6	*5.85*

Based on the simulated surge results, different analyses is conduced to study different aspect of the temporal evolution of storm surge. Herein we present sea level rise induced changes in peak surge timing, local surge time series, and evolution of inundation extent.

4.3 Results and Discussion

4.3.1 Surge Timing and Temporal Evolution

One important variable that can change with sea level rise is the peak surge timing. In certain areas, peak surge may arrive earlier than present-day situation, making evacuation more urgently. Figure 4.2 shows different peak surge arrival times for the slow (storm 7) and fast (storm 1) storms under the 0 and 1.95 m sea level rise scenarios as representative results.

First, for both the slow storm and the fast storm, peak surge arrival shifted 2-3 hours earlier in Sarasota Bay. Specifically, for the fast storm, peak surge arrives approximately 3 hours after landfall under present-day sea level, but 0-1 hour after landfall with a 1.95 m sea level rise. This is true for all the fast storms simulated (storm 1-5). For the slow storm, peak surge arrives about 1 hour after landfall under present-day sea level, but 2 hours before landfall with a 1.95 m sea level rise - this peak surge can hit coastal communities unexpectedly early because peak surge actually arrives before storm landfall. What makes this early time shift more dangerous is that for all the storms simulated, peak surges within Sarasota Bay experience a superlinear response to sea level rise. That is, peak surge with sea level rise is about 1-2 m higher than the summation of present-day surge and 1.95 m sea level rise value. The reasons for the peak surge timing change within Sarasota Bay is probably associated with the sea level rise induced failure of the front barrier island Longboat Key's surge blocking function. While in the present-day situation, Longboat Key can block most of the surge water at the open coast. Rather, most surge water gets into Sarasota Bay through openings in the north and south. Increased sea levels decrease the relative height of Longboat Key. This allows ocean storm surge to more easily overtop Longboat Key when surge comes in.

The same phenomenon also occurs in Boca Ciega Bay in the north.

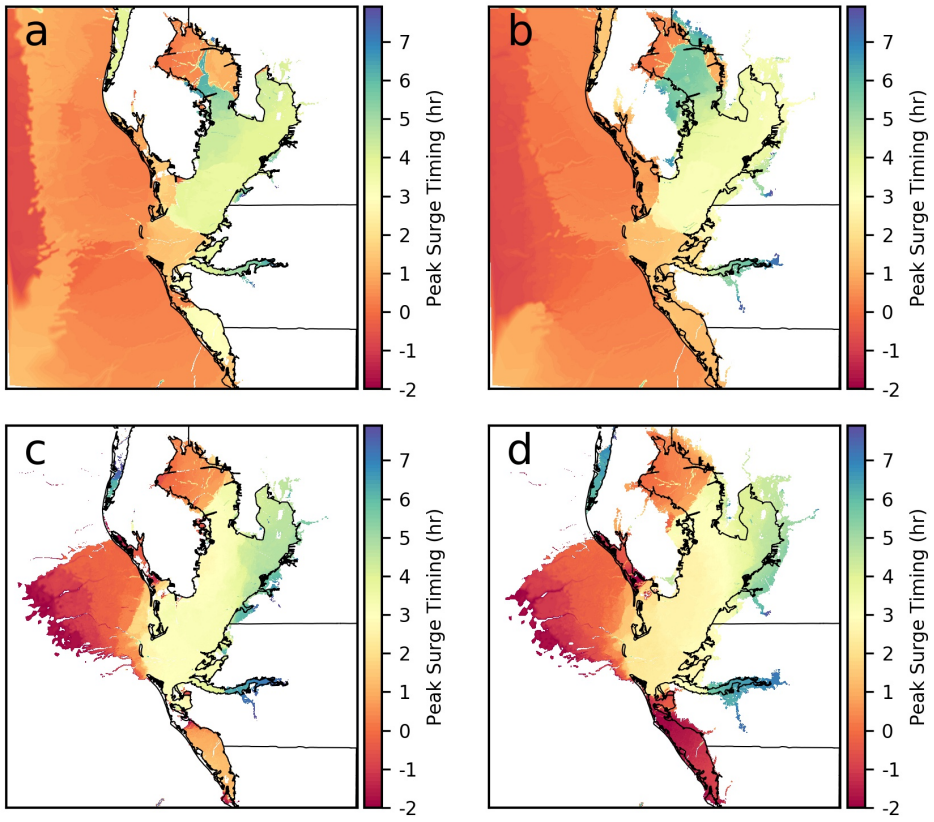

Figure 4.2: Peak Surge Timing

Further inland, Old Tampa Bay experiences rather different peak surge timing change with sea level rise from what is observed at Sarasota and Boca Ciega Bay right behind the first coastline. In Old Tampa Bay, peak surge timing does not change for different sea level rise scenarios for the slow storm, while peak surge timing is delayed by 5-6 hours with a 1.95 m sea level rise for the fast storm. The cause for this peak surge timing delay can be best explained by examining local surge time series and is presented below.

To further investigate surge timing and temporal evolution, surge time series at specific geographical locations can show what happens temporally at local levels more clearly. To this end, surge time series data at 60 locations along the coastlines encompassing the Tampa

Bay region area for all the simulated storms and SLR scenarios is analyzed. Results at four locations are shown herein as representative results (Figure 4.3). Overall, surge evolution

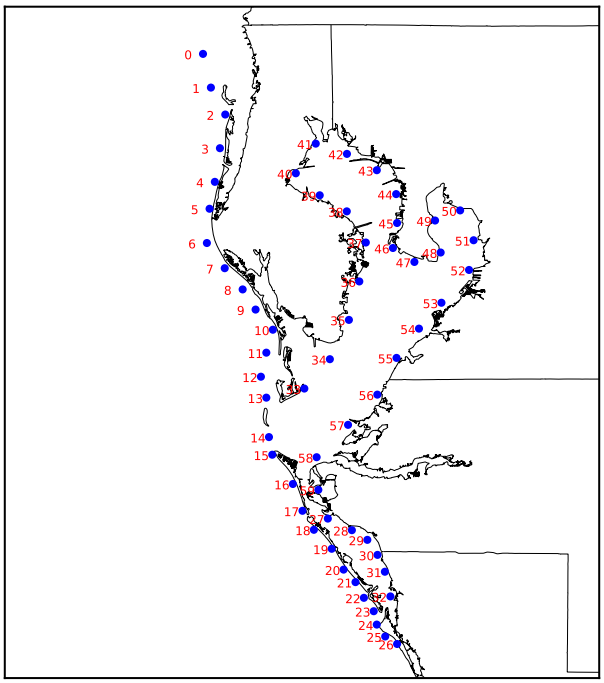

Figure 4.3: Map showing the 60 locations along the coastlines encompassing the Tampa Bay region study area.

prior to peak (i.e., the forerunner surge) is less sensitive to sea level rise than peak surge in almost all of the open coast locations (locations 0-26 in Figure 4.3). For example, at location 20 in front of Sarasota Bay (Figure 4.4), while peak surge responds slightly sublinearly (DNL less than 0.2 m) to sea level rise for all the simulated storms, no sublinearity or at most a weak sublinearity is observed in the surge evolution preceding peak surge. This means that prior to peak, surge evolution with sea level rise will only be slightly less than, if not the same as, the exact summation of the forerunner surge magnitude and the sea level rise amount in the open coast. This nearly linear surge evolution response to sea level rise is an evident that storm-induced shelf waves are not strongly influenced by sea level rise.

Results are more complicated within Sarasota Bay. At location 28 in the north opening of Sarasota Bay (Figure 4.5), results show that while the slower moving storms (storm 6&7) have a superlinear response to sea level rise, no significant change is observed for the surge evolution before peak surge, similar to the response of the open coast locations. However, for the fast moving storms (storm 1-5), peak surge responds superlinerly to sea level rise while surge before peak responds sublinearly, meaning with increased mean sea level, surge level will more rapidly increase right before the storm's landfall. Take storm 3 as an example, surge magnitude increases from 0.2 m to 3.8 m within 12 hours right before storm landfall in present-day situation. With a 1.95 m sea level rise for the same storm 3, surge magnitude increases from 0.1 m to 4.8 m within 12 hours before landfall, at a rate more than 2 m/day faster than the present-day situation. On the contrary, at Location 33 in the south opening of Sarasota Bay, the slow moving storms exhibit no obvious nonlinearity for the peak surge, but the whole temporal evolution moves forward in time, meaning both forerunner surge and peak surge arrive earlier than in the present-day scenario.

The above described changes of surge time series within Sarasota Bay are most likely related to the fact that beside the aforementioned more overtopping, increased mean sea level also makes it easier for water to get into Sarasota Bay through New Pass (the south opening), but easier for water to escape from the north opening. Therefore, for the fast storms, water piles up faster than it can escape through the north opening, creating a more dramatical increase of water right before storm landfall. For the slow storms, locations near the south opening experiences surge evolution more and more like open coast locations in a more timely fashion, thus the early shift of surge time series.

Within Old Tampa Bay, Figure 4.7 shows that the locally generated surge (first peak) is larger than the magnitude of the open coast surge wave (second peak) for all but the largest

storm (storm 5). But with sea level rise, locally generated surge decreases and traveled open coast surge increases; thus the former is smaller than the latter, causing the significant delay of the peak surge timing. Specifically, peak surge corresponds well with storm landfall at present-day situation within Old Tampa Bay for the fast storm, but can arrive as late as 6 hours after storm landfall with sea level rise. This is because the geographical feature of Old Tampa Bay allows the bay coastline to directly encounter the counterclockwise storm wind at landfall, when the strong onshore wind blows water up within Old Tampa Bay, creating a large, locally generated surge. After landfall, piled up surge water at the open coast gradually travel into the Bay, creating another surge water. Sea level rise changes the relative magnitudes of these two surges. Specifically, with sea level rise, the magnitude of the locally generated surge at storm landfall decreases due to increased water depth, and the magnitude of the traveled open coast surge arriving hours after storm landfall increases due to less dampening from increased water depth. The larger locally generally surge in present-day situation then becomes the smaller surge under sea level rise scenarios, resulting in the peak surge timing delay within Old Tampa Bay.

4.3.2 Inundation Extent

Another important aspect is how the temporal evolution of the inundation extent changes with sea level rise. It is intuitive that the inundation extent will be larger with sea level rise, but how the inundation evolves with time is still unstudied. To that end, we select 8 cross-shore transects in the study area (Figure 4.8) and examine how the inundation extent as well as inundation depth develops with time. The most significant changes are observed for transect 5 and transect 8. The inundation extent temporal evolution at transect 8 for the slow storm (storm 7) is plotted in Figure 4.9 as an illustrative example. Firstly, it is shown

that sea level rise can make certain places to inundate earlier than present-day situation for all storms. For Figure 4.9 specifically, transect 8 gets inundated almost 12 hours before landfall, about 10 hours earlier than the present-day situation for the slow storm (storm 7). While the red dashed lines indicate the different wet-dry boundaries under different sea level rise scenarios, a simple but convenient assumption would be that the inundation over the wet-dry boundaries would be the same if the storm meteorological forcing is the same. However, it is seen that the inundation extent evolution due to storm surge is different at different sea level rise scenarios. For the present-day condition, water flows inland for about 0.1 km. With 1.95 m sea level rise, using the same storm meteorological forcing, water can flow inland for 1.1 km. The flood depth also increases for about 2 m. This 1 km more inundation extent can flood hundreds of more houses considering the residential density in this area, posing a danger to a lot more people and more properties.

We further calculate the hourly total inundated area and examine how the inundation extent evolves temporally in the study area as a whole, and how this evolution changes as sea levels rise. Our results show that for all the simulated storms, increased sea levels increases the total inundation area as expected (Figure 4.10). However, this increase is not well explained by simply shifting the flood plain by the SLR amount (Figure 4.11). It is observed that for all the fast moving storms (storms 1-5), increasing sea levels decrease the maximum surge-induced inundation areas. For the two slow storms (storms 6&7), the surge-induced inundation area increases as mean sea levels increase. This means under sea level rise scenarios, in terms of inundation extent, the response of slow storms are more dangerous because they tend to inundate more areas. For the slowest storm (storm 7), the increased inundation area is approximately 500 km^2. Furthermore, the temporal gradient of inundation area (Figure 4.12) shows the peak inundation increasing rate decreases with sea level rise, but the timing of the peak inundation increasing rate shifts earlier in time with sea level rise. This means

with sea level rise, more and more surge block features fail and water can flow more freely at an earlier stage, making the fasted inundation happen early.

4.4 Conclusions

A range of synthetic storms are simulated in the Tampa Bay region, West Florida, with four sea level rise scenarios considered for each storm. Surge anomaly time series and inundation extent are examined to investigate how sea level rise will impact them. Based on our results, peak surge can arrive 2-3 earlier in Sarasota Bay and 6 hours later in Old Tampa Bay with sea level rise.

Secondly, surge evolution prior to peak can respond differently to peak surge. The most noteworthy changes happen at the north opening of Sarasota Bay for fast storms, where surge more rapidly increase prior to peak; and at the south opening (New Pass) of Sarasota Bay, where the whole surge evolution profile shift about 3 hours earlier in time, resulting in larger forerunner surge and earlier peak surge timing.

Thirdly, surge induced inundation extent increases linearly with sea level rise and can be 1 km wider than expected in Sarasota Bay for the slow storm.

Lastly, storm surge induced inundation area changes with sea level rise, and is the maximum in the present-day situation in the study area.

All of the above mentioned situations can be dangerous since surge water can hit the residential areas unexpectedly early or late, stranding people and damaging properties. Future coastal planning and engineering should thus not only take into account the impact of sea

level rise on peak surge and probabilistic surge, but also the impact of sea level rise on the temporal evolution of storm surge.

Acknowledgements

The authors wish to thank the Federal Emergency Management Agency for providing the ADCIRC mesh and other data. This material is based upon work supported by the National Science Foundation under Grant Nos. CMMI-1206271 and EAR-1630099. This work used resources of Advanced Research Computing at Virginia Tech.

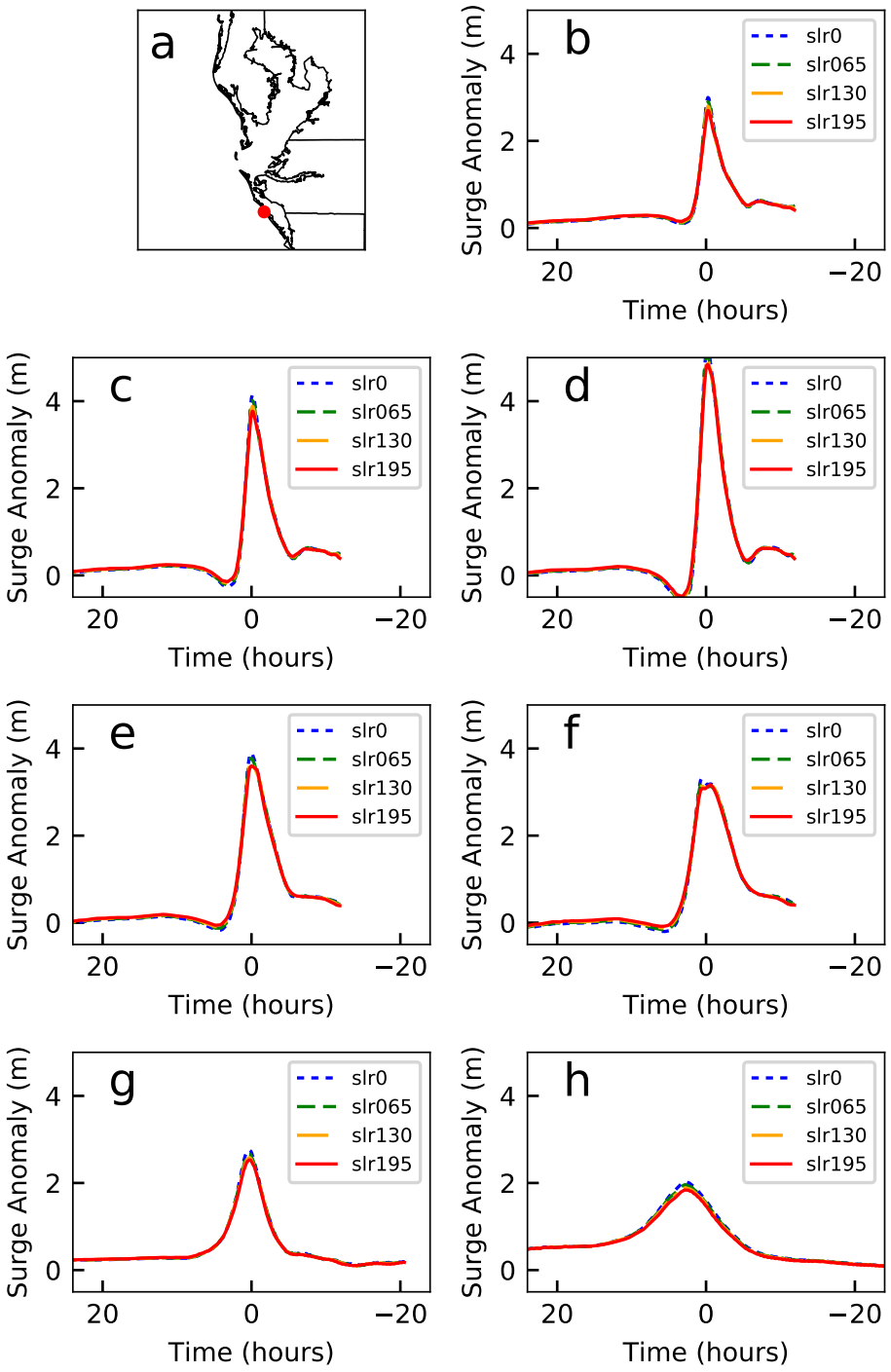

Figure 4.4: Surge anomaly subtracted by sea level rise amount time series at Location 20 on the open coast. Each subplot is for a) Location map, b) storm 1, c) storm 2, d) storm 3, e) storm 4, f) storm 5, g) storm 6, and g) storm 7.

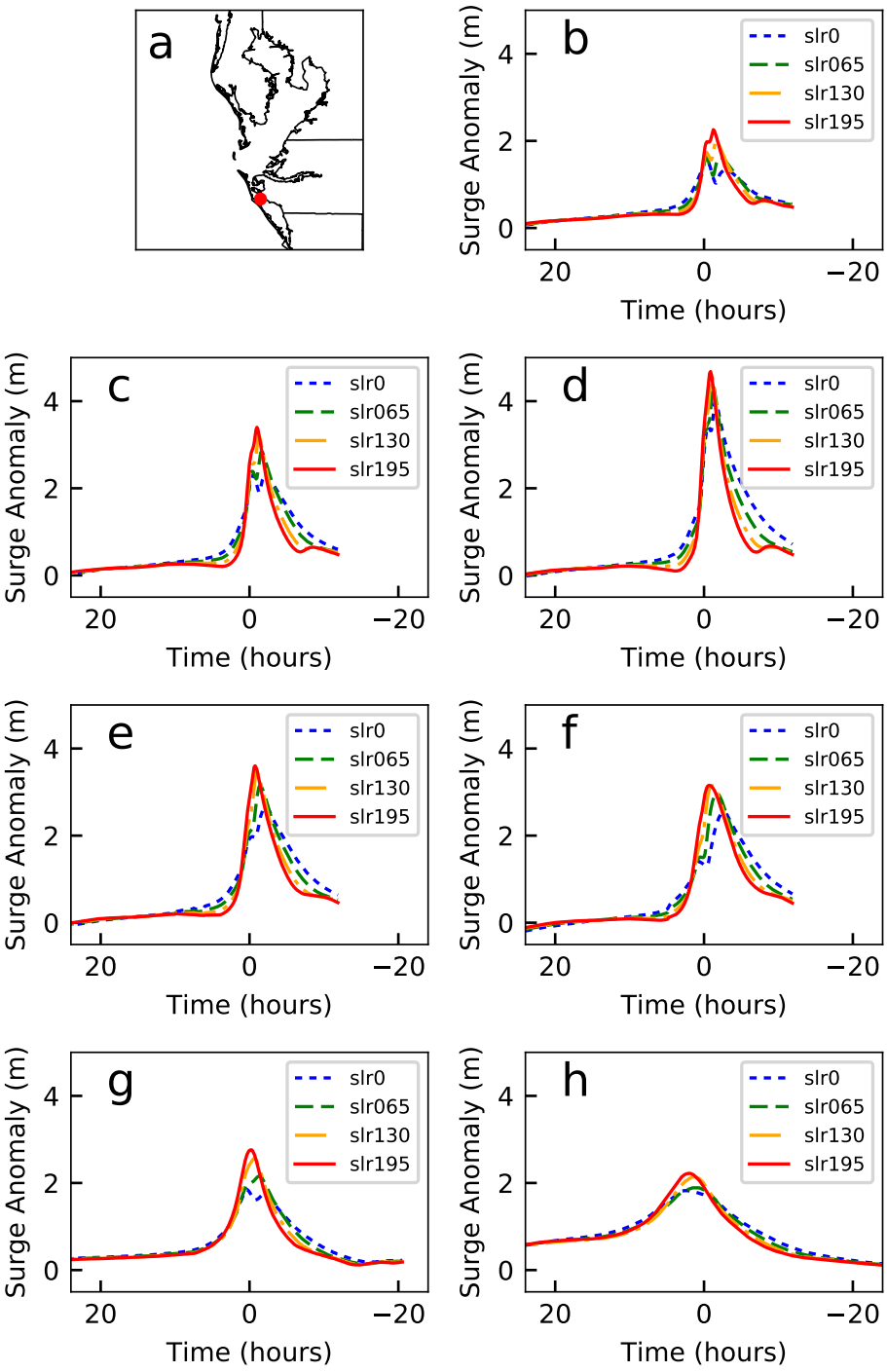

Figure 4.5: Surge anomaly subtracted by sea level rise amount time series at Location 28 in the north opening of Sarasota Bay. Each subplot is for a) Location map, b) storm 1, c) storm 2, d) storm 3, e) storm 4, f) storm 5, g) storm 6, and g) storm 7.

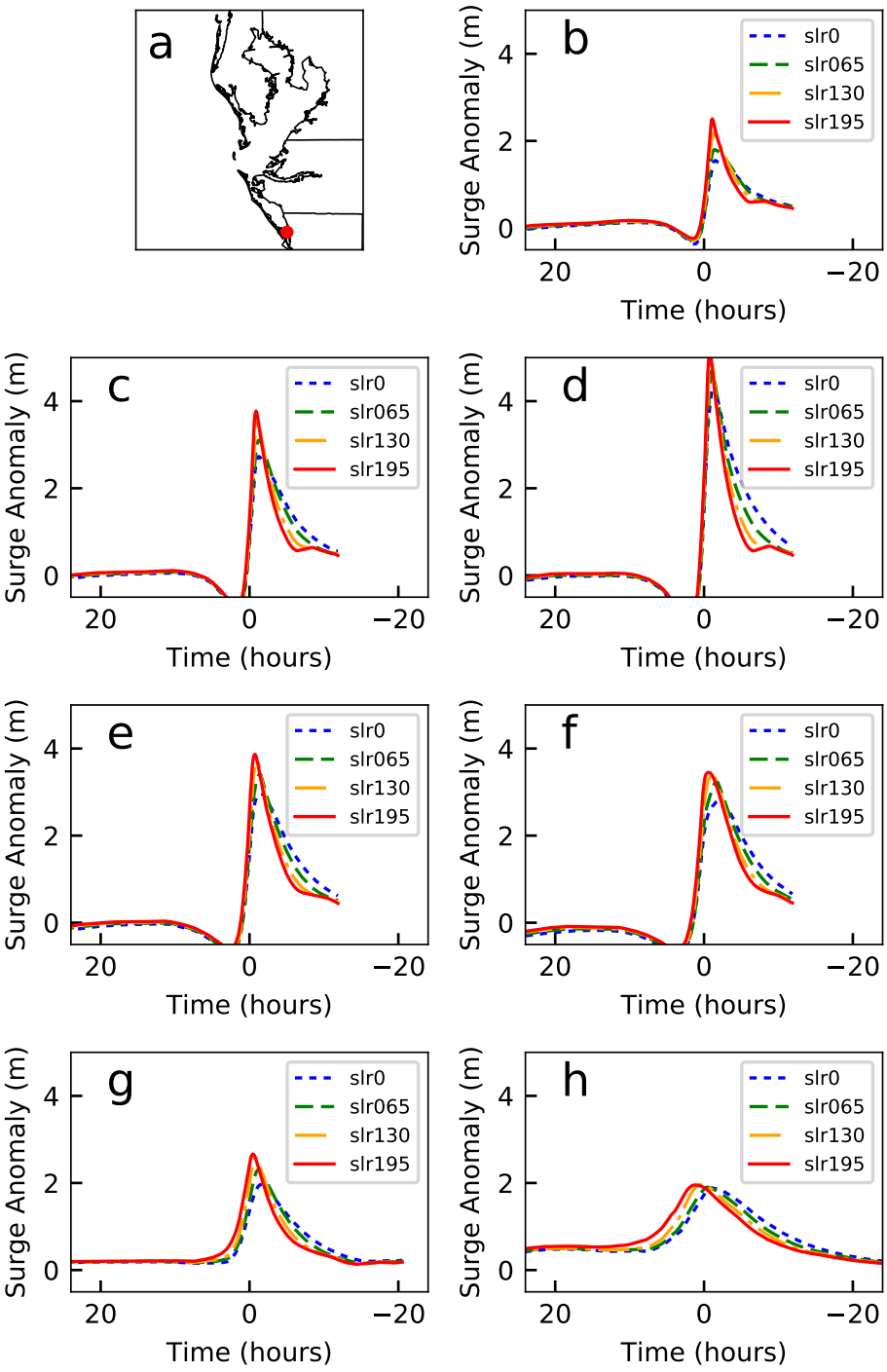

Figure 4.6: Surge anomaly subtracted by sea level rise amount time series at Location 33 in the south opening of Sarasota Bay. Each subplot is for a) Location map, b) storm 1, c) storm 2, d) storm 3, e) storm 4, f) storm 5, g) storm 6, and g) storm 7.

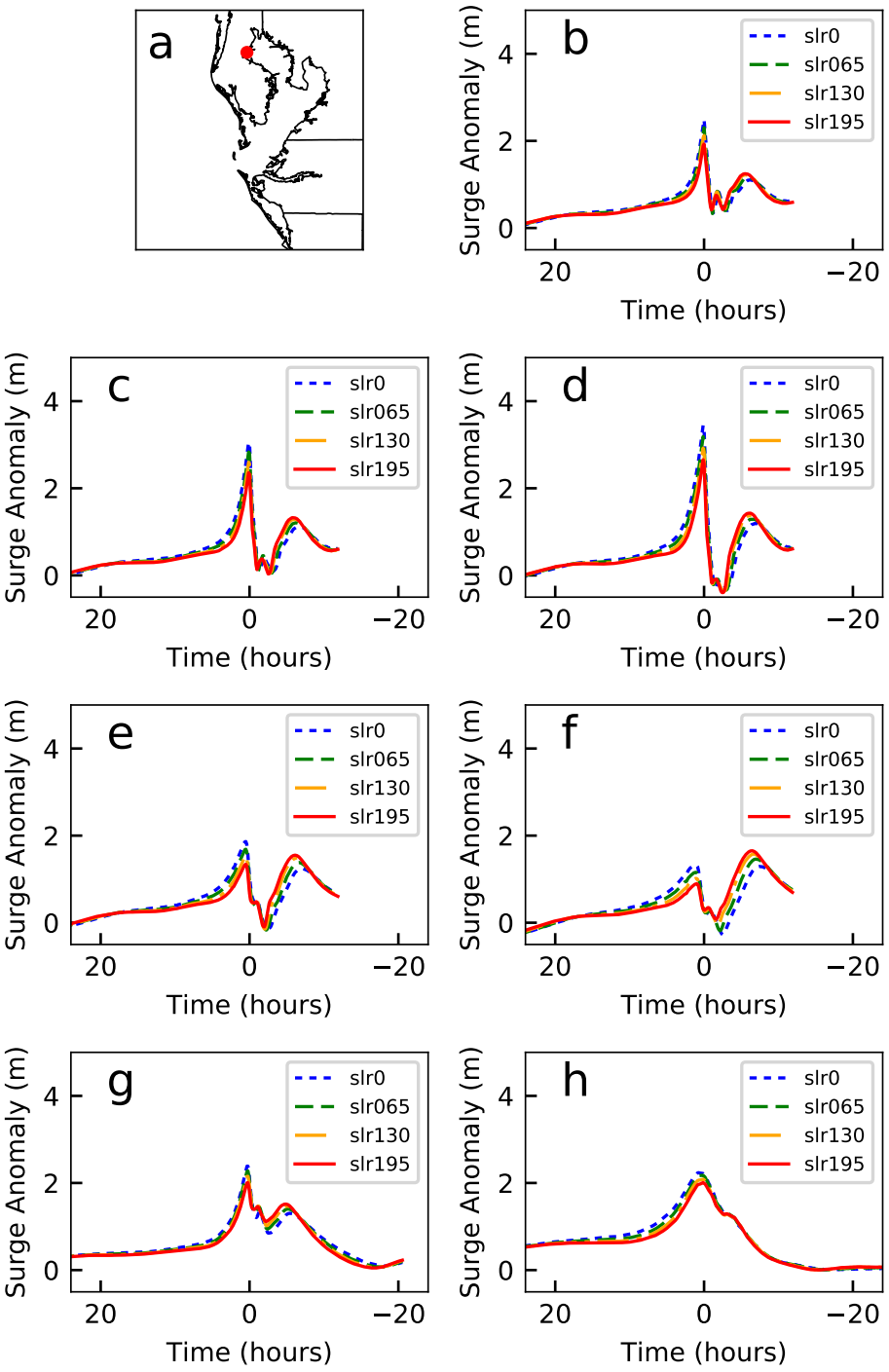

Figure 4.7: Surge anomaly subtracted by sea level rise amount time series at Location 41 on the open coast. Each subplot is for a) Location map, b) storm 1, c) storm 2, d) storm 3, e) storm 4, f) storm 5, g) storm 6, and g) storm 7.

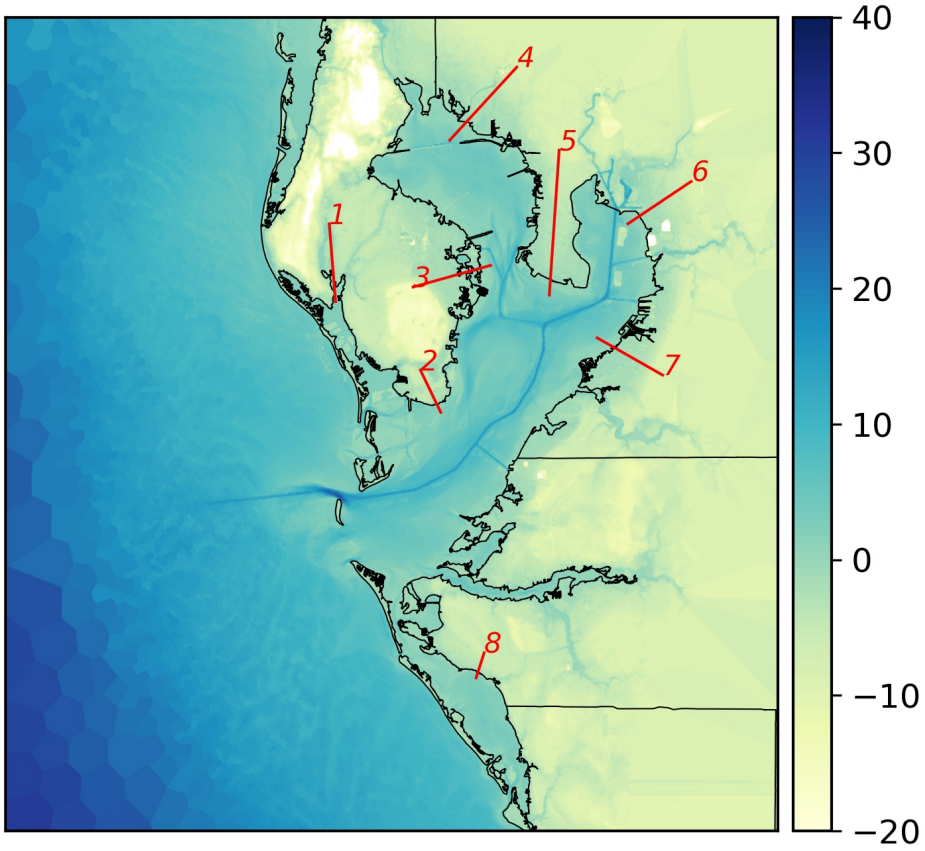

Figure 4.8: Study area map with overland cross-shore transects of interest.

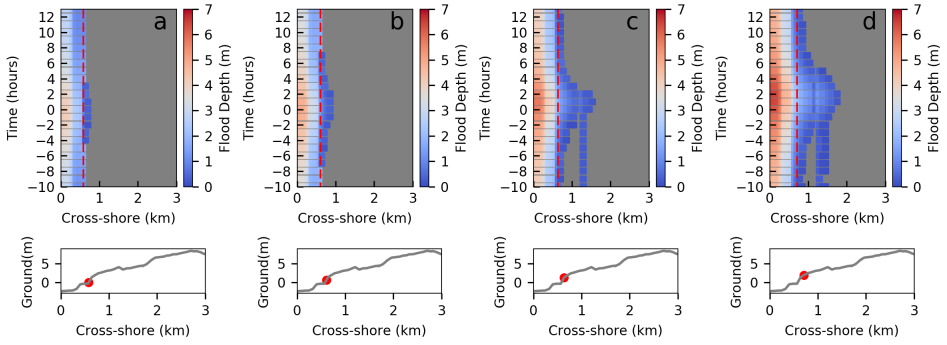

Figure 4.9: Inundation extent temporal evolution at transect 8 for the slow storm (storm 7). The first row shows the inundated nodes along transect 8 developed with time, color coded by the flood depth, for a) present-day sea level, b) 0.65 m sea level rise, c) 1.30 sea level rise and d)1.95 sea level rise. The second row shows the ground elevation along transect 8. The red dashed lines in the first row plots and the red dots in the second row plots show the mean sea level.

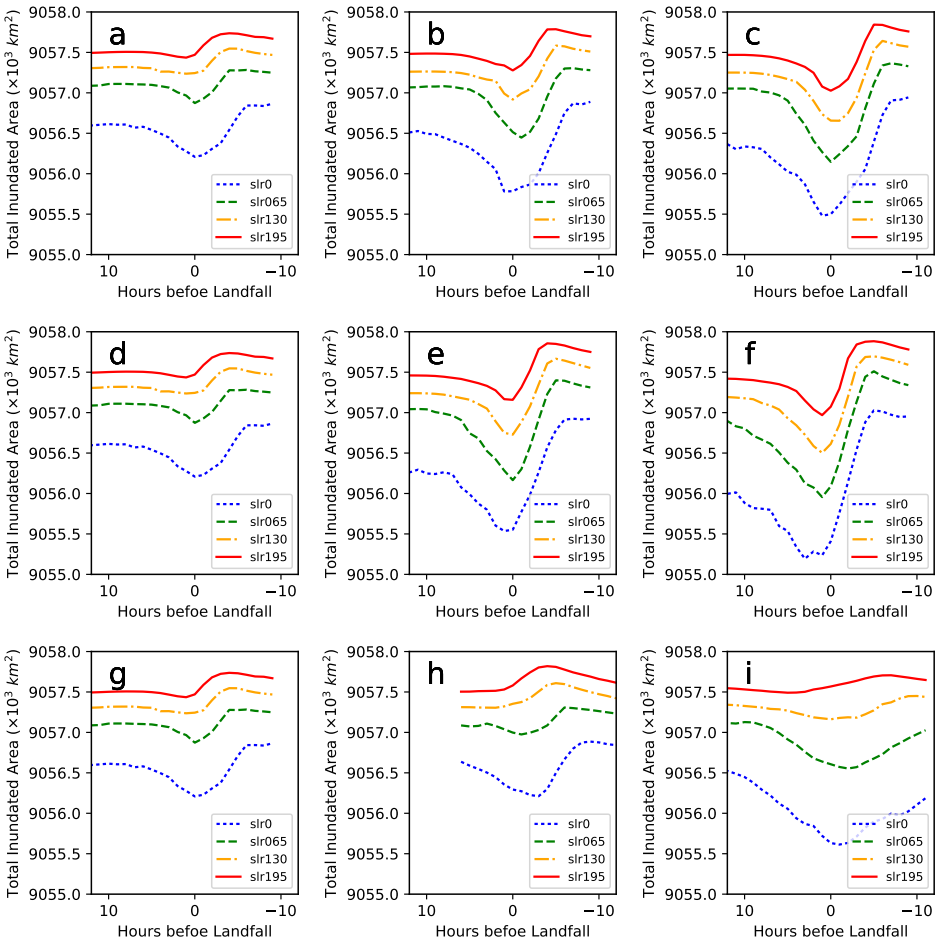

Figure 4.10: Total inundation area temporal evolution under different sea level rise scenarios. Row one is for storms with increasing intensity (storm 1, 2, and 3 in subplot a), b) and c)). Row two is for storms with increasing size (storm 1, 4, and 5 in subplot d), e) and f)). Row three is for storms with decreasing speed (storm 1, 6, and 7 in subplot g), h) and i).

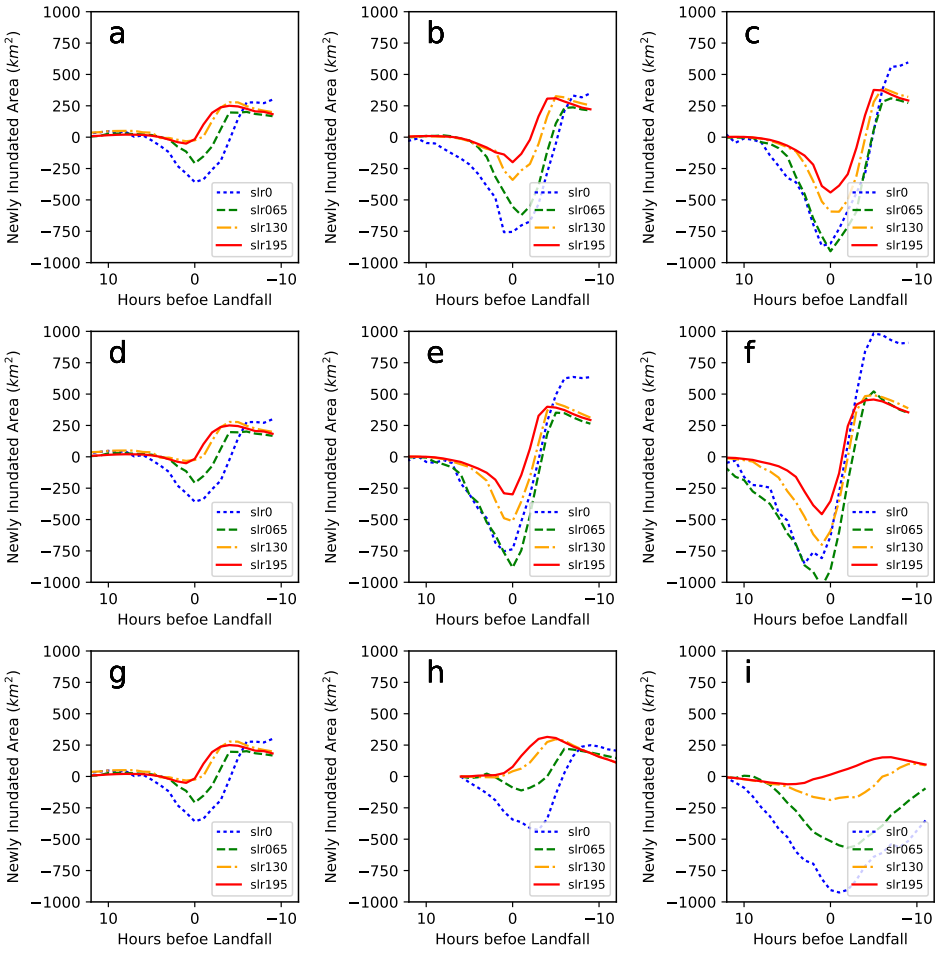

Figure 4.11: Surge-induced inundation area temporal evolution under different sea level rise scenarios. Row one is for storms with increasing intensity (storm 1, 2, and 3 in subplot a), b) and c)). Row two is for storms with increasing size (storm 1, 4, and 5 in subplot d), e) and f)). Row three is for storms with decreasing speed (storm 1, 6, and 7 in subplot g), h) and i).

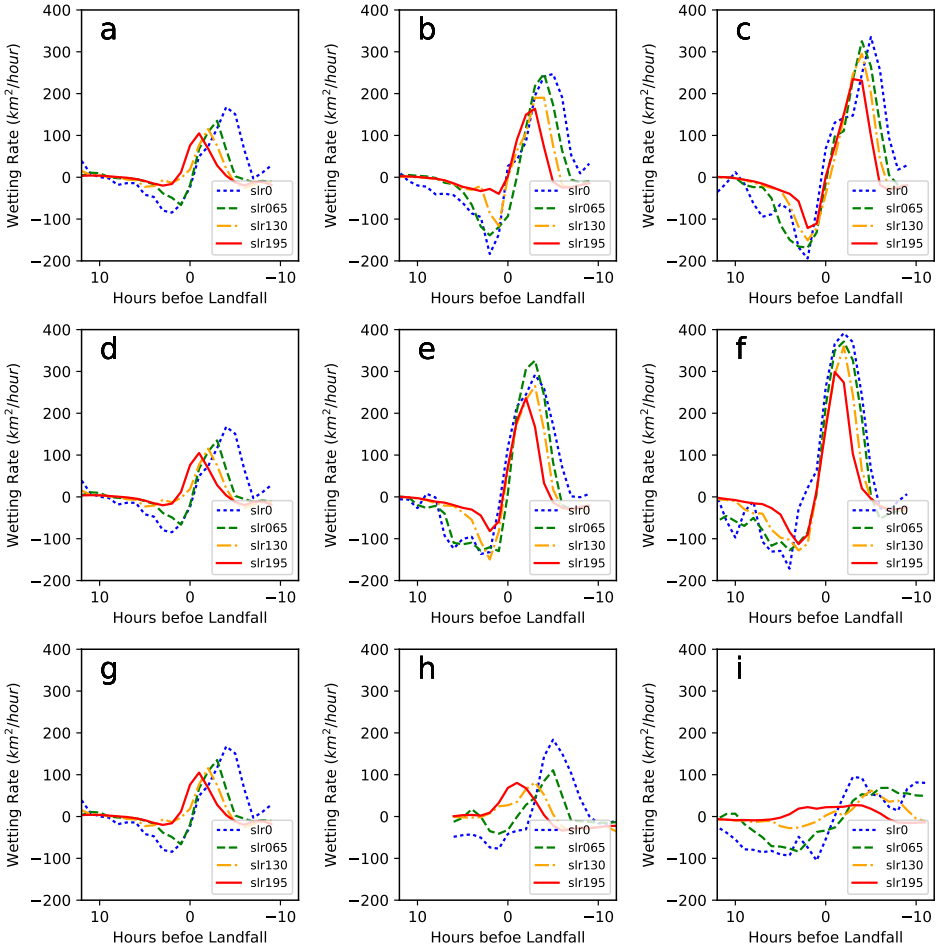

Figure 4.12: Inundation area increasing rate. Row one is for storms with increasing intensity (storm 1, 2, and 3 in subplot a), b) and c)). Row two is for storms with increasing size (storm 1, 4, and 5 in subplot d), e) and f)). Row three is for storms with decreasing speed (storm 1, 6, and 7 in subplot g), h) and i).

Chapter 5

Conclusions

Forerunner surge in advance of a tropical cyclone landfall can leave people stranded, preventing evacuation and rescue. With projected global sea level rise, probabilistic surge hazard and forerunner surge hazard will change, which should be studied and considered for coastal planning and engineering. In this dissertation, we investigate numerical modeling results using ADCIRC+SWAN/STWAVE and consider a large range of synthetic storms and sea level rise scenarios. We characterize and predict forerunner surge. We study how the probabilistic surge hazard and how the forerunner surge will change under sea level rise. The main conclusions are:

- A set of scaling laws are developed for fast and reliable forerunner surge forecasts, as well as the identification of the range of storm conditions in which a large forerunner surge is possible. These scaling laws prove that slow-moving, large, and intense storms have the most potential for generating dangerous forerunner surges, because such storms generate and sustain the strong alongshore currents needed to produce Ekman setup (Chapter 2).

- Probabilistic surge with sea level rise can be 1.0 m larger than the exact summation of the two in part of the study area. The response of individual storm's surge to sea level rise is a poor indicator of the probabilistic surge hazard's response. When considering

large sea level rise scenarios, complex topography, and large surge events, the impact of sea level rise on the probabilistic surge hazard is hard to predict and should be investigated more carefully (Chapter 3).

- Different temporal evolution phase of storm surge (e.g., forerunner surge, peak surge) responds differently to sea level rise for storms with different forward speed at regions with different topographic features(Chapter 4).

The forerunner surge forecasting equations developed in Chapter 2 also have the potential to be incorporated into coastal flooding warning systems, and may be used to aid emergency managers and communities in evacuation planning and execution. Because the predictive equations herein are physically based, they are also of high value to regions worldwide influenced by tropical cyclones and surge threats, such as the Pacific coasts of southeast Asia, west and east Australia (Eliot and Pattiaratchi, 2010), and the Bay of Bengal. In developing regions that lack sophisticated computer modeling, the methods and findings can be applied directly to gauge data or limited simulation results to better characterize forerunner surge threat. While the meteorological community has studied and come to consensus that future tropical cyclones will be more intense under global warming (IPCC, 2014; Knutson et al., 2010), little attention has been given to the influence of global warming on storm size and forward speed. Yet, such investigations are in critical need given the significant influence of size and forward speed on forerunner surge.

The results presented in Chapter 3 have important implications for surge-SLR response studies. All in all, when considering low SLR scenarios and small surge events in regions where no obvious watercourse change under SLR, the "bathtub" method of assuming no nonlinearity with surge-SLR response may be useful. On the contrary, when considering higher SLR, large surge events, and/or regions with obvious watercourse change under SLR

(e.g., failure of flow obstructions, wider flow openings, and limited drainage paths), surge is expected to respond more nonlinearly and less predictably to SLR. In these cases, the influence of surge-SLR nonlinearities should be examined more closely to guide future planning, engineering, and mitigation measures, ensuring more robust coastal development and more resilient coastal communities.

In Chapter 4, the impact of sea level rise on the temporal evolution of storm surge is further studied in the Tampa Bay region, West Florida. Based on our results, with future sea level rise, peak surge can arrive 3-6 hours earlier or later in different geographical areas, depending on the mechanisms of surge temporal evolution there. Surge evolution prior to peak (also defined as forerunner surge in Chapter 2) can respond differently to peak surge. Specifically, with sea level rise, in part of the study area, surge can more rapidly increase prior to peak; in some other part of the study area, larger forerunner surge and earlier peak surge timing may happen. Moreover, surge induced inundation extent increases nonlinearly with sea level rise and can be 1 km wider than expected for the slow storm. All of the above mentioned situations can be dangerous since surge water can hit the residential areas unexpectedly early or late, stranding people and damaging properties. Future coastal planning and engineering should thus not only take into account the impact of sea level rise on peak surge and probabilistic surge, but also the impact of sea level rise on the temporal evolution of storm surge.

Future work to improve understanding and ability to predict forerunner surge should consider, for example, the influence of locally generated surge in coastal bays, tides, improved parameterized wind model, and vertical flow structure of Ekman setup. For instance, Using the two-layer model GeoClaw in an idealized storm scenario, the physics of forerunner surge may be better captured and the prediction accuracy of our scaling laws may be improved

(Mandli, 2011). Future studies on the impact of sea level rise on surge hazard should consider the integration of hydrodynamic model, long-term coastal evolution model, anthropogenic response model, and climate change model. Other physical processes including rainfall and storm-induced erosion during tropical cyclones may also be considered.

Bibliography

John Atkinson, Jane McKee Smith, and Christopher Bender. Sea-Level Rise Effects on Storm Surge and Nearshore Waves on the Texas Coast: Influence of Landscape and Storm Characteristics. *Journal of Waterway, Port, Coastal, and Ocean Engineering*, 139(2):98–117, March 2013. doi: 10.1061/(ASCE)WW.1943-5460.0000187. URL http://ascelibrary.org/doi/full/10.1061/%28ASCE%29WW.1943-5460.0000187.

Lauren N. Augustin, Jennifer L. Irish, and Patrick Lynett. Laboratory and numerical studies of wave damping by emergent and near-emergent wetland vegetation. *Coastal Engineering*, 56(3):332–340, March 2009. ISSN 0378-3839. doi: 10.1016/j.coastaleng.2008.09.004. URL http://www.sciencedirect.com/science/article/pii/S037838390800152X.

Robbie Berg. Tropical cyclone report: Hurricane Ike 1-14 September 2008. Technical report, National Hurricane Center, 2009.

M. V. Bilskie, S. C. Hagen, S. C. Medeiros, and D. L. Passeri. Dynamics of sea level rise and coastal flooding on a changing landscape. *Geophysical Research Letters*, 41(3): 927–934, February 2014. ISSN 1944-8007. doi: 10.1002/2013GL058759. URL http://onlinelibrary.wiley.com/doi/10.1002/2013GL058759/abstract.

Eric S. Blake, Christopher W. Landsea, and Ethan J. Gibney. The deadliest, costliest, and most intense United States tropical cyclones from 1851 to 2010 (and other frequently requested hurricane facts). NOAA Technical Memorandum NWS NHC-6, 2011. URL https://www.census.gov/history/pdf/nws-nhc-6.pdf.

N. Booij, L. H. Holthuijsen, and R. C. Ris. The "SWAN" wave model for shallow water.

Coastal Engineering Proceedings, 1(25), 1996. ISSN 2156-1028. URL https://journals.tdl.org/icce/index.php/icce/article/view/5257.

Peter D. Bromirski, Arthur J. Miller, Reinhard E. Flick, and Guillermo Auad. Dynamical suppression of sea level rise along the Pacific coast of North America: Indications for imminent acceleration. *Journal of Geophysical Research: Oceans*, 116(C7):C07005, July 2011. ISSN 2156-2202. doi: 10.1029/2010JC006759. URL http://onlinelibrary.wiley.com/doi/10.1029/2010JC006759/abstract.

Mahunnop Bunpapong, Robert O. Reid, and Robert E. Whitaker. An Investigation of Hurricane-Induced Forerunner Surge in the Gulf of Mexico. Technical report, September 1985.

S. Bunya, J. C. Dietrich, J. J. Westerink, B. A. Ebersole, J. M. Smith, J. H. Atkinson, R. Jensen, D. T. Resio, R. A. Luettich, C. Dawson, V. J. Cardone, A. T. Cox, M. D. Powell, H. J. Westerink, and H. J. Roberts. A High-Resolution Coupled Riverine Flow, Tide, Wind, Wind Wave, and Storm Surge Model for Southern Louisiana and Mississippi. Part I: Model Development and Validation. *Monthly Weather Review*, 138 (2):345–377, February 2010a. ISSN 0027-0644. doi: 10.1175/2009MWR2906.1. URL http://journals.ametsoc.org/doi/abs/10.1175/2009MWR2906.1.

S Bunya, J Cl Dietrich, JJ Westerink, BA Ebersole, JM Smith, JH Atkinson, R Jensen, DT Resio, RA Luettich, C Dawson, et al. A high-resolution coupled riverine flow, tide, wind, wind wave, and storm surge model for southern louisiana and mississippi. part i: Model development and validation. *Monthly weather review*, 138(2):345–377, 2010b.

John A. Church and Neil J. White. A 20th century acceleration in global sea-level rise. *Geophysical Research Letters*, 33(1):L01602, January 2006. ISSN 1944-8007. doi: 10.1029/

2005GL024826. URL http://onlinelibrary.wiley.com/doi/10.1029/2005GL024826/abstract.

John A. Church and Neil J. White. Sea-Level Rise from the Late 19th to the Early 21st Century. *Surveys in Geophysics*, 32(4-5):585–602, September 2011. ISSN 0169-3298, 1573-0956. doi: 10.1007/s10712-011-9119-1. URL https://link.springer.com/article/10.1007/s10712-011-9119-1.

John A. Church, P.U. Clark, A. Cazenave, J.M. Gregory, S. Jevrejeva, A. Levermann, M.A. Merrifield, G.A. Milne, R.S. Nerem, P.D. Nunn, A.J. Payne, W.T. Pfeffer, D. Stammer, and A.S. Unnikrishnan. Sea Level Change. Technical report, Cambridge University Press, Cambridge, United Kingdom and New York, NY, USA, 2013.

Cialone, Alison S. Grzegorzewski, David J. Mark, Mary A. Bryant, and Thomas C. Massey. Coastal-Storm Model Development and Water-Level Validation for the North Atlantic Coast Comprehensive Study. *Journal of Waterway, Port, Coastal, and Ocean Engineering*, 143(5):04017031, September 2017. doi: 10.1061/(ASCE)WW.1943-5460.0000408. URL http://ascelibrary.org/doi/full/10.1061/%28ASCE%29WW.1943-5460.0000408.

Mary A. Cialone, T. C. Massey, Mary E. Anderson, Alison S. Grzegorzewski, Robert E. Jensen, Alan Cialone, David J. Mark, Kimberly C. Pevey, Brittany L. Gunkel, and Tate O. McAlpin. North Atlantic Coast Comprehensive Study (NACCS) Coastal Storm Model Simulations: Waves and Water Levels. Technical report, August 2015.

Isaac M. Cline. Relation of changes in storm tides on the coast of the gulf of mexico to the center and movement of hurricanes. *Monthly Weather Review*, 48(3):127–146, March 1920. ISSN 0027-0644. doi: 10.1175/1520-0493(1920)48<127:ROCIST>2.0.CO;2. URL http://journals.ametsoc.org/doi/abs/10.1175/1520-0493(1920)48%3C127:ROCIST%3E2.0.CO%3B2.

Daniel Benjamin Gardiner Collins, RL Bras, and Gregory E Tucker. Modeling the effects of vegetation-erosion coupling on landscape evolution. *Journal of Geophysical Research: Earth Surface*, 109(F3), 2004.

Robert M. DeConto and David Pollard. Contribution of Antarctica to past and future sea-level rise. *Nature*, 531(7596):591–597, March 2016. ISSN 0028-0836. doi: 10.1038/nature17145. URL http://www.nature.com/nature/journal/v531/n7596/full/nature17145.html.

J. C. Dietrich, S. Tanaka, J. J. Westerink, C. N. Dawson, R. A. Luettich, M. Zijlema, L. H. Holthuijsen, J. M. Smith, L. G. Westerink, and H. J. Westerink. Performance of the Unstructured-Mesh, SWAN+ADCIRC Model in Computing Hurricane Waves and Surge. *Journal of Scientific Computing*, 52(2):468–497, August 2012. ISSN 0885-7474, 1573-7691. doi: 10.1007/s10915-011-9555-6. URL http://link.springer.com/article/10.1007/s10915-011-9555-6.

J. C. Dietrich, C. N. Dawson, J. M. Proft, M. T. Howard, G. Wells, J. G. Fleming, R. A. Luettich, J. J. Westerink, Z. Cobell, M. Vitse, H. Lander, B. O. Blanton, C. M. Szpilka, and J. H. Atkinson. Real-Time Forecasting and Visualization of Hurricane Waves and Storm Surge Using SWAN+ADCIRC and FigureGen. In *Computational Challenges in the Geosciences*, pages 49–70. Springer, New York, NY, 2013. doi: 10.1007/978-1-4614-7434-0_3. URL https://link.springer.com/chapter/10.1007/978-1-4614-7434-0_3.

J.C. Dietrich. *Development and application of coupled hurricane wave and surge models for southern Louisiana*. PhD thesis, UNIVERSITY OF NOTRE DAME, 2011. URL http://gradworks.umi.com/34/36/3436250.html.

JC Dietrich, S Bunya, JJ Westerink, BA Ebersole, JM Smith, JH Atkinson, R Jensen, DT Resio, RA Luettich, C Dawson, et al. A high-resolution coupled riverine flow, tide,

wind, wind wave, and storm surge model for southern louisiana and mississippi. part ii: Synoptic description and analysis of hurricanes katrina and rita. *Monthly Weather Review*, 138(2):378–404, 2010.

Matthew Eliot and Charitha Pattiaratchi. Remote forcing of water levels by tropical cyclones in southwest Australia. *Continental Shelf Research*, 30(14):1549–1561, August 2010. ISSN 0278-4343. doi: 10.1016/j.csr.2010.06.002. URL http://www.sciencedirect.com/science/article/pii/S0278434310001949.

C. Fanelli, P. Fanelli, and D. Wolcott. NOAA Water Level and Meteorological Data Report—Hurricane Sandy. Technical report, US Department of Commerce, National Oceanic and Atmospheric Administration, National Ocean Service Center for Operational Oceanographic Products and Services, 2013.

E.B. Garriott. West Indian hurricane of September 1–12, 1900. *Monthly Weatther Review*, 28(9):371–377, September 1900.

Bob Glahn, Arthur Taylor, Nicole Kurkowski, and Wilson A. Shaffer. The role of the SLOSH model in National Weather Service storm surge forecasting. *National Weather Digest*, 33 (1):3–14, 2009.

Juan L González and Torbjörn E Tornqvist. Coastal louisiana in crisis: Subsidence or sea level rise? *EOS, Transactions American Geophysical Union*, 87(45):493–498, 2006.

Francis P. Ho and Vance A. Myers. *Joint probability method of tide frequency analysis applied to Apalachicola Bay and St. George Sound, Florida /*. U.S. Dept. of Commerce, National Oceanic and Atmospheric Administration, National Weather Service ;, Silver Spring, Md. :, 1975.

Greg J. Holland. An Analytic Model of the Wind and Pressure Profiles in Hurricanes.

Monthly Weather Review, 108(8):1212–1218, August 1980. ISSN 0027-0644. doi: 10.1175/1520-0493(1980)108<1212:AAMOTW>2.0.CO;2. URL http://journals.ametsoc.org/doi/abs/10.1175/1520-0493(1980)108%3C1212:AAMOTW%3E2.0.CO%3B2.

Sythesis report IPCC. *IPCC, 2014: Climate Change 2014: Synthesis Report. Contribution of Working Groups I, II and III to the Fifth Assessment Report of the Intergovernmental Panel on Climate Change*. IPCC, Geneva, Switzerland, 2014. ISBN 978-92-9169-143-2. URL http://www.ipcc.ch/report/ar5/syr/.

Jennifer L. Irish and Donald T. Resio. Method for Estimating Future Hurricane Flood Probabilities and Associated Uncertainty. *Journal of Waterway, Port, Coastal, and Ocean Engineering*, 139(2):126–134, March 2013. doi: 10.1061/(ASCE)WW.1943-5460.0000157. URL http://ascelibrary.org/doi/full/10.1061/%28ASCE%29WW.1943-5460.0000157.

Jennifer L. Irish, Donald T. Resio, and Jay J. Ratcliff. The Influence of Storm Size on Hurricane Surge. *Journal of Physical Oceanography*, 38(9):2003–2013, September 2008. ISSN 0022-3670. doi: 10.1175/2008JPO3727.1. URL http://journals.ametsoc.org/doi/full/10.1175/2008JPO3727.1.

Jennifer L. Irish, Donald T. Resio, and Mary A. Cialone. A surge response function approach to coastal hazard assessment. Part 2: Quantification of spatial attributes of response functions. *Natural Hazards*, 51(1):183–205, March 2009. ISSN 0921-030X, 1573-0840. doi: 10.1007/s11069-009-9381-4. URL http://link.springer.com/article/10.1007/s11069-009-9381-4.

Jennifer L Irish, Donald T Resio, and David Divoky. Statistical properties of hurricane surge along a coast. *Journal of Geophysical Research: Oceans*, 116(C10), 2011a.

Jennifer L. Irish, Youn Kyung Song, and Kuang-An Chang. Probabilistic hurricane surge forecasting using parameterized surge response functions. *Geophysical Research Letters*,

38(3):L03606, February 2011b. ISSN 1944-8007. doi: 10.1029/2010GL046347. URL http://onlinelibrary.wiley.com/doi/10.1029/2010GL046347/abstract.

Jennifer L. Irish, Alison Sleath, Mary A. Cialone, Thomas R. Knutson, and Robert E. Jensen. Simulations of Hurricane Katrina (2005) under sea level and climate conditions for 1900. *Climatic Change*, 122(4):635–649, February 2014. ISSN 0165-0009, 1573-1480. doi: 10.1007/s10584-013-1011-1. URL https://link.springer.com/article/10.1007/s10584-013-1011-1.

Gaofeng Jia, Alexandros A. Taflanidis, Norberto C. Nadal-Caraballo, Jeffrey A. Melby, Andrew B. Kennedy, and Jane M. Smith. Surrogate modeling for peak or time-dependent storm surge prediction over an extended coastal region using an existing database of synthetic storms. *Natural Hazards*, 81(2):909–938, March 2016. ISSN 0921-030X, 1573-0840. doi: 10.1007/s11069-015-2111-1. URL https://link.springer.com/article/10.1007/s11069-015-2111-1.

Andrew B. Kennedy, Uriah Gravois, Brian C. Zachry, Joannes J. Westerink, Mark E. Hope, J. Casey Dietrich, Mark D. Powell, Andrew T. Cox, Richard A. Luettich, and Robert G. Dean. Origin of the Hurricane Ike forerunner surge. *Geophysical Research Letters*, 38 (8):L08608, April 2011. ISSN 1944-8007. doi: 10.1029/2011GL047090. URL http://onlinelibrary.wiley.com/doi/10.1029/2011GL047090/abstract.

Richard D. Knabb, Jamie R. Rhome, and Daniel P. Brown. Tropical Cyclone Report: Hurricane Katrina. Technical Report, NOAA National Hurricane Center, August 2005.

Thomas R. Knutson, John L. McBride, Johnny Chan, Kerry Emanuel, Greg Holland, Chris Landsea, Isaac Held, James P. Kossin, A. K. Srivastava, and Masato Sugi. Tropical cyclones and climate change. *Nature Geosci*, 3(3):157–163, March 2010. ISSN 1752-0894. doi: 10.1038/ngeo779. URL http://dx.doi.org/10.1038/ngeo779.

Robert E. Kopp, Radley M. Horton, Christopher M. Little, Jerry X. Mitrovica, Michael Oppenheimer, D. J. Rasmussen, Benjamin H. Strauss, and Claudia Tebaldi. Probabilistic 21st and 22nd century sea-level projections at a global network of tide-gauge sites. *Earth's Future*, 2(8):2014EF000239, August 2014. ISSN 2328-4277. doi: 10.1002/2014EF000239. URL http://onlinelibrary.wiley.com/doi/10.1002/2014EF000239/abstract.

Alfredo Mahar Francisco Lagmay, Rojelee P. Agaton, Mark Allen C. Bahala, Jo Brianne Louise T. Briones, Krichi May C. Cabacaba, Carl Vincent C. Caro, Lea L. Dasallas, Lia Anne L. Gonzalo, Christine N. Ladiero, John Phillip Lapidez, Maria Theresa Francia Mungcal, Jose Victor R. Puno, Michael Marie Angelo C. Ramos, Joy Santiago, John Kenneth Suarez, and Judd P. Tablazon. Devastating storm surges of Typhoon Haiyan. *International Journal of Disaster Risk Reduction*, 11(Supplement C):1–12, March 2015. ISSN 2212-4209. doi: 10.1016/j.ijdrr.2014.10.006. URL http://www.sciencedirect.com/science/article/pii/S2212420914000922.

Christopher W. Landsea and James L. Franklin. Atlantic Hurricane Database Uncertainty and Presentation of a New Database Format. *Monthly Weather Review*, 141(10):3576–3592, January 2013. ISSN 0027-0644. doi: 10.1175/MWR-D-12-00254.1. URL http://journals.ametsoc.org/doi/abs/10.1175/MWR-D-12-00254.1.

Christopher W. Landsea, David A. Glenn, William Bredemeyer, Michael Chenoweth, Ryan Ellis, John Gamache, Lyle Hufstetler, Cary Mock, Ramon Perez, Ricardo Prieto, Jorge Sánchez-Sesma, Donna Thomas, and Lenworth Woolcock. A Reanalysis of the 1911–20 Atlantic Hurricane Database. *Journal of Climate*, 21(10):2138–2168, May 2008. ISSN 0894-8755. doi: 10.1175/2007JCLI1119.1. URL http://journals.ametsoc.org/doi/abs/10.1175/2007JCLI1119.1.

Ning Lin, Kerry Emanuel, Michael Oppenheimer, and Erik Vanmarcke. Physically based

assessment of hurricane surge threat under climate change. *Nature Climate Change; London*, 2(6):462–467, June 2012. ISSN 1758678X. doi: http://dx.doi.org/10.1038/nclimate1389. URL https://search.proquest.com/docview/1039387051/abstract/CB2331198364CCCPQ/1.

R.A. Luettich, J.J. Westerink, and Norman W. Scheffner. ADCIRC: An Advanced Three-Dimensional Circulation Model for Shelves, Coasts, and Estuaries. Report 1. Theory and Methodology of ADCIRC-2ddi and ADCIRC-3dl. No. CERC-TR-DRP-92-6. Technical report, COASTAL ENGINEERING RESEARCH CENTER VICKSBURG MS, 1992.

Kyle T. Mandli. *Finite Volume Methods for the Multilayer Shallow Water Equations with Applications to Storm Surges*. Ph.D., University of Washington, United States – Washington, 2011. URL https://search.proquest.com/docview/906801969/abstract/DFD87D6B6F0D4990PQ/1.

J. X. Mitrovica and G. A. Milne. On the origin of late Holocene sea-level highstands within equatorial ocean basins. *Quaternary Science Reviews*, 21(20):2179–2190, November 2002. ISSN 0277-3791. doi: 10.1016/S0277-3791(02)00080-X. URL http://www.sciencedirect.com/science/article/pii/S027737910200080X.

Steven L. Morey, Stephen Baig, Mark A. Bourassa, Dmitry S. Dukhovskoy, and James J. O'Brien. Remote forcing contribution to storm-induced sea level rise during Hurricane Dennis. *Geophysical Research Letters*, 33(19):L19603, October 2006. ISSN 1944-8007. doi: 10.1029/2006GL027021. URL http://onlinelibrary.wiley.com/doi/10.1029/2006GL027021/abstract.

Norberto C. Nadal-Caraballo, Jefferey A. Melby, Victor M. Gonzalez, and Andrew T. Cox. North Atlantic Coast Comprehensive Study—Coastal Storm Hazards from Virginia to

Maine. Technical Report ERDC/CHL TR-15-5, 228 p, U.S. Army Engineer Research and Development Center, Vicksburg, Mississippi, 2015.

NHC. National Hurricane Center tropical cyclone advisory, 2017. URL http://www.nhc.noaa.gov/archive/.

Robert J. Nicholls and Anny Cazenave. Sea-Level Rise and Its Impact on Coastal Zones. *Science*, 328(5985):1517–1520, June 2010. ISSN 0036-8075, 1095-9203. doi: 10.1126/science.1185782. URL http://science.sciencemag.org/content/328/5985/1517.

A. W. Niedoroda, D. T. Resio, G. R. Toro, D. Divoky, H. S. Das, and C. W. Reed. Analysis of the coastal Mississippi storm surge hazard. *Ocean Engineering*, 37(1): 82–90, January 2010. ISSN 0029-8018. doi: 10.1016/j.oceaneng.2009.08.019. URL http://www.sciencedirect.com/science/article/pii/S0029801809002157.

NOAA. National Coastal Population Report: Population Trends from 1970 to 2020. Technical report, March 2013. URL https://coast.noaa.gov/digitalcoast/training/population-report.html.

NOAA. Tides and currents, 2017. URL https://tidesandcurrents.noaa.gov/.

Adam Parris, Peter Bromirski, Dan Cayan, Mary Culver, John Hall, Radley Horton, Kevin Knuuti, Richard Moss, Jayantha Obeysekera, Abby Sallenger, and Jeremy Weiss. Global sea level rise scenarios for the United States National Climate Assessment. NOAA Tech Memo, 2012.

Joseph Pedlosky. *Geophysical Fluid Dynamics*. Springer Science & Business Media, 1990. ISBN 978-1-4612-4650-3. Google-Books-ID: iIbTBwAAQBAJ.

Mark D. Powell and Timothy A. Reinhold. Tropical Cyclone Destructive Potential by Integrated Kinetic Energy. *Bulletin of the American Meteorological Society*, 88(4):

513–526, April 2007. ISSN 0003-0007. doi: 10.1175/BAMS-88-4-513. URL http://journals.ametsoc.org/doi/abs/10.1175/BAMS-88-4-513.

Stefan Rahmstorf. A Semi-Empirical Approach to Projecting Future Sea-Level Rise. *Science*, 315(5810):368–370, January 2007. ISSN 0036-8075, 1095-9203. doi: 10.1126/science.1135456. URL http://science.sciencemag.org/content/315/5810/368.

RAMMB. Aircraft-based Tropical Cyclone Surface Wind Analysis, 2017. URL http://rammb.cira.colostate.edu/products/tc_realtime/archive_sub_products.asp?product=airctcwa&storm_identifier=AL092017.

Donald T Resio and Jennifer L Irish. Tropical cyclone storm surge risk. *Current Climate Change Reports*, 1(2):74–84, 2015.

Donald T. Resio, Jennifer Irish, and Mary Cialone. A surge response function approach to coastal hazard assessment – part 1: basic concepts. *Natural Hazards*, 51(1):163–182, April 2009. ISSN 0921-030X, 1573-0840. doi: 10.1007/s11069-009-9379-y. URL http://link.springer.com/article/10.1007/s11069-009-9379-y.

Donald T. Resio, Jennifer L. Irish, Joannes J. Westerink, and Nancy J. Powell. The effect of uncertainty on estimates of hurricane surge hazards. *Natural Hazards*, 66(3):1443–1459, April 2013. ISSN 0921-030X, 1573-0840. doi: 10.1007/s11069-012-0315-1. URL https://link.springer.com/article/10.1007/s11069-012-0315-1.

Antonia Sebastian, Jennifer Proft, J. C. Dietrich, Wei Du, Philip B. Bedient, and Clint N. Dawson. Characterizing hurricane storm surge behavior in Galveston Bay using the SWAN + ADCIRC model. *Coastal Engineering*, 88:171–181, June 2014. ISSN 0378-3839. doi: 10.1016/j.coastaleng.2014.03.002. URL http://www.sciencedirect.com/science/article/pii/S0378383914000556.

Jane M. Smith, Ann R. Sherlock, and Donald T. Resio. STWAVE: Steady-State Spectral Wave Model User's Manual for STWAVE, Version 3.0. Technical report, February 2001.

Jane McKee Smith, Mary A. Cialone, Ty V. Wamsley, and Tate O. McAlpin. Potential impact of sea level rise on coastal surges in southeast Louisiana. *Ocean Engineering*, 37 (1):37–47, January 2010. ISSN 0029-8018. doi: 10.1016/j.oceaneng.2009.07.008. URL http://www.sciencedirect.com/science/article/pii/S0029801809001784.

W.P. Stewart. Hurricane of August 16-17, 1915. report of the local Galveston forecaster, Galveston, TX, 1915.

William V Sweet, Robert E Kopp, Christopher P Weaver, Jayantha Obeysekera, Radley M Horton, E Robert Thieler, and Chris Zervas. Global and regional sea level rise scenarios for the united states. 2017.

Alexandros A. Taflanidis, Andrew B. Kennedy, Joannes J. Westerink, Jane Smith, Kwok Fai Cheung, Mark Hope, and Seizo Tanaka. Rapid assessment of wave and surge risk during landfalling hurricanes: probabilistic approach. *Journal of Waterway, Port, Coastal, and Ocean Engineering*, 139(3):171–182, 2013.

Arthur A. Taylor and Bob Glahn. Probabilistic guidance for hurricane storm surge. *19th Conference on probability and statistics*, 74, 2008.

Edward F. Thompson and Vincent J. Cardone. Practical Modeling of Hurricane Surface Wind Fields. *Journal of Waterway, Port, Coastal, and Ocean Engineering*, 122(4):195–205, 1996. ISSN 0733-950X. doi: 10.1061/(ASCE)0733-950X(1996)122:4(195). URL http://dx.doi.org/10.1061/(ASCE)0733-950X(1996)122:4(195).

Ann B Tihansky. Sinkholes, west-central florida. *Land subsidence in the United States: US geological survey circular*, 1182:121–140, 1999.

G. R. Toro, A. W. Niedoroda, C. W. Reed, and D. Divoky. Quadrature-based approach for the efficient evaluation of surge hazard. *Ocean Engineering*, 37(1):114–124, 2010a. ISSN 0029-8018. doi: 10.1016/j.oceaneng.2009.09.005. URL http://www.sciencedirect.com/science/article/pii/S0029801809002248.

G. R. Toro, D. T. Resio, D. Divoky, A.W. Niedoroda, and Chris Reed. Efficient joint-probability methods for hurricane surge frequency analysis. *Ocean Engineering*, 37(1): 125–134, 2010b. ISSN 0029-8018. doi: 10.1016/j.oceaneng.2009.09.004. URL http://www.sciencedirect.com/science/article/pii/S0029801809002236.

Martin Vermeer and Stefan Rahmstorf. Global sea level linked to global temperature. *Proceedings of the National Academy of Sciences*, 106(51):21527–21532, December 2009. ISSN 0027-8424, 1091-6490. doi: 10.1073/pnas.0907765106. URL http://www.pnas.org/content/106/51/21527.

Joannes J Westerink, Richard A Luettich, Jesse C Feyen, John H Atkinson, Clint Dawson, Hugh J Roberts, Mark D Powell, Jason P Dunion, Ethan J Kubatko, and Hasan Pourtaheri. A basin-to channel-scale unstructured grid hurricane storm surge model applied to southern louisiana. *Monthly weather review*, 136(3):833–864, 2008.

Jonathan D. Woodruff, Jennifer L. Irish, and Suzana J. Camargo. Coastal flooding by tropical cyclones and sea-level rise. *Nature*, 504(7478):44–52, December 2013. ISSN 00280836. URL http://search.proquest.com/docview/1468675513/abstract/4BD6797BBE514735PQ/1.

Appendices

Appendix A

Historical Observations of Surge Time Series

Table A.1: Hurricane track parameters averaged between 6 to 24 hours before landfall. Data source: (a) NHC (2017), (b) Powell and Reinhold (2007), (c) Nadal-Caraballo et al. (2015), (d) Sebastian et al. (2014), and (e) RAMMB (2017).

Hurricane	$\Delta p(hPa)$	$R(m)$	$V_f(km/h)$
Isabel (2003)	$56^{(a)}$	$87^{(b)}$	$20^{(a)}$
Sandy (2012)	$65^{(a)}$	$135^{(c)}$	$26^{(a)}$
Ike (2008)	$63^{(a)}$	$74^{(d)}$	$18^{(a)}$
Harvey (2017)	$56^{(a)}$	$26^{(e)}$	$17^{(a)}$

Table A.2: Dimensionless curve fitting coefficients for Equation 2.3

	Curve Fitting Coefficints		
Location	a	b	c
VA-1	5.44	1.24	-0.11
VA-2	4.36	0.96	-0.09
NJ-1	2.70	-0.38	0.11
NJ-2	3.21	-0.49	0.05
TX-1	5.96	0.42	0.31
TX-2	6.30	0.24	0.18

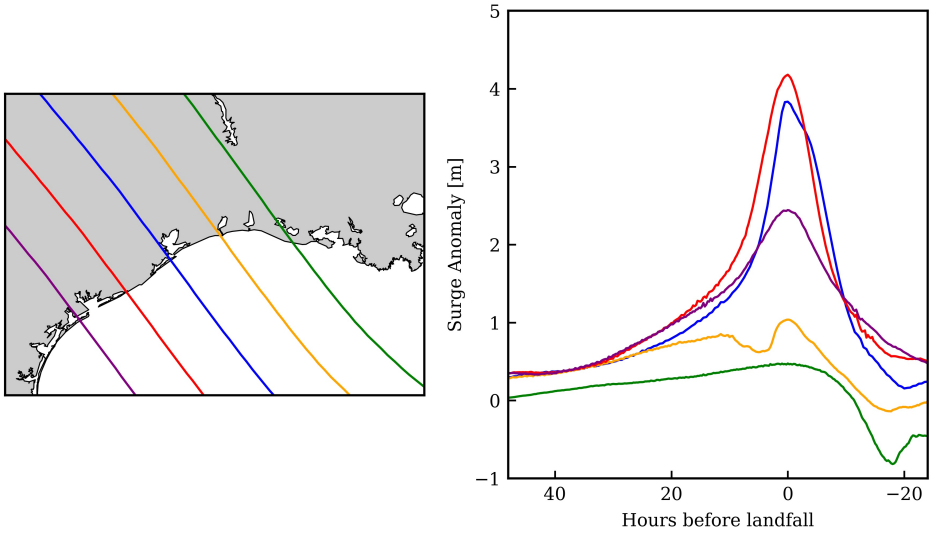

Figure A.1: Tracks and surge time series for an Ike-like synthetic tropical cyclone that is shifting 100-km or 200-km to the south or north.

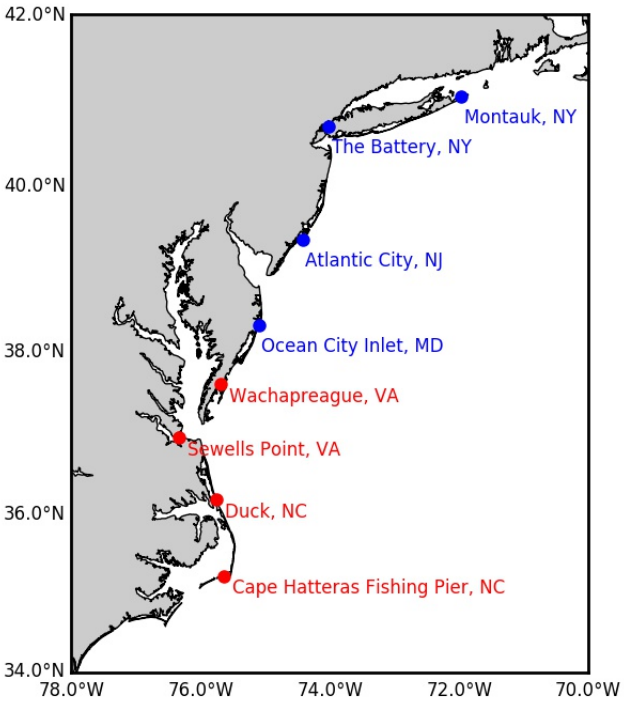

Figure A.2: Map showing locations of NOAA (2017) observational water level data presented for Hurricane Sandy (2012, blue circles) and Hurricane Isabel (2003, red circles).

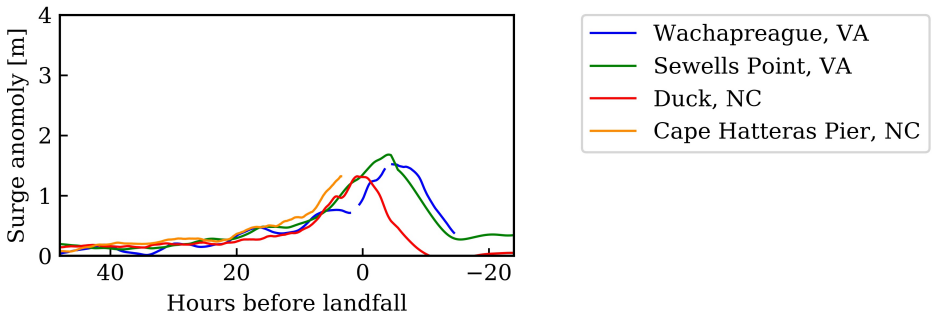

Figure A.3: Observed water level anomaly time series (NOAA, 2017) for Hurricane Isabel (2003); locations shown in Figure A.2 .

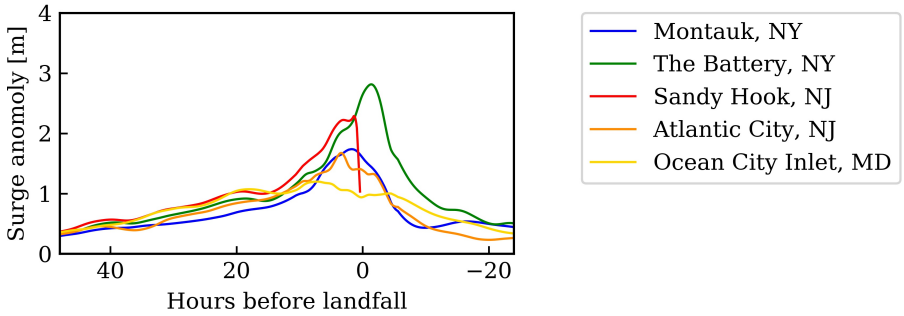

Figure A.4: Observed water level anomaly time series (NOAA, 2017) for Hurricane Sandy (2012); locations shown in Figure A.2.

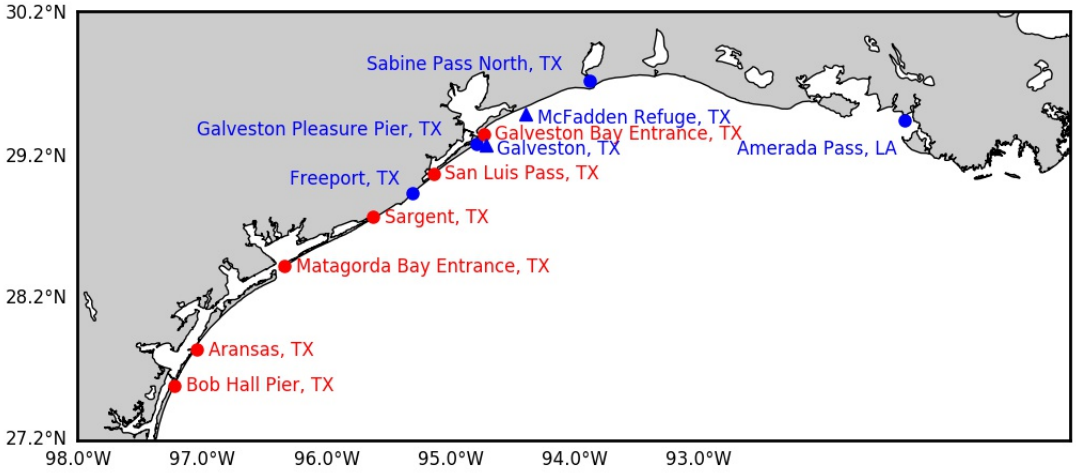

Figure A.5: Map showing locations of observational water level data presented for Hurricane Ike (2008, blue circles and triangles) and Hurricane Harvey (2017, red circles). NOAA (2017) stations are circles and Kennedy et al. (2011) stations are triangles.

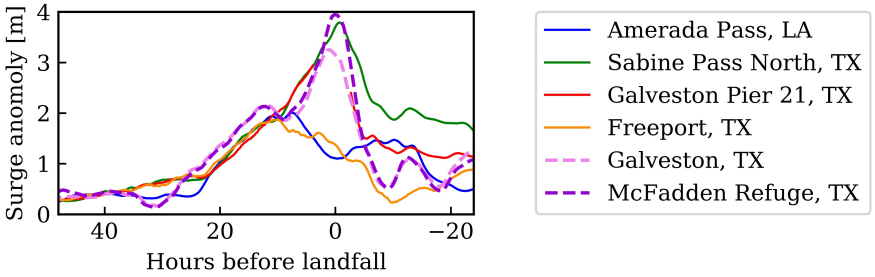

Figure A.6: Observed water level anomaly time series (NOAA, 2017; Kennedy et al., 2011); locations shown in Figure A.5.

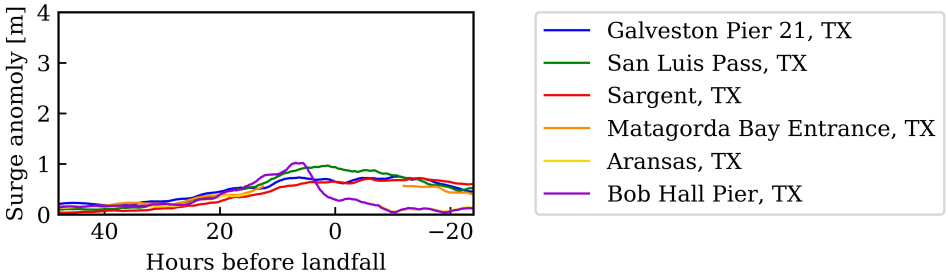

Figure A.7: Observed water level anomaly time series (NOAA, 2017) for Hurricane Harvey (2017); locations shown in Figure Figure A.5.

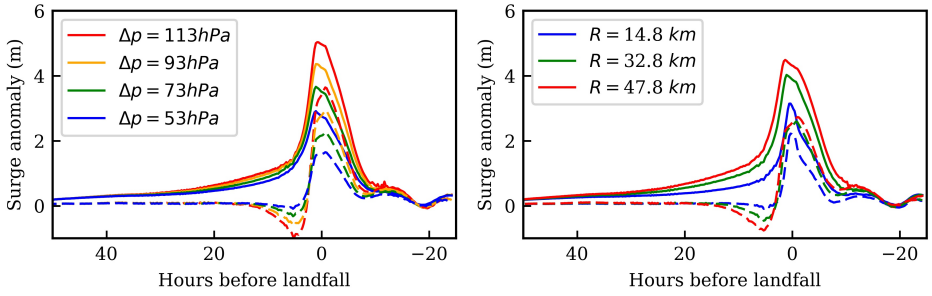

Figure A.8: Simulated surge time series with (solid lines) and without (dashed lines) Coriolis forcing for tropical cyclones along track TX-T2 with a 5.66 m/s V_f and (a) 32.8 km R, (b) 73 hPa Δp.

Appendix B

Probabilistic Surge Hazard Maps and Sensitivity Tests

This Appendix includes sensitivity tests of how coastal morphology evolution may impact the surge hazard response to sea level rise. Also included are figures showing 2% AEP and 0.2% AEP surge values in the study area (Tampa, Florida), and the contribution-weighted mean value (defined in main text) of pressure deficit, storm radius, and heading under present sea level and under 1.95-m sea level rise.

Long-term Coastal Evolution

SLR induced coastal evolution, such as dune degradation and vegetation loss, also introduce changes in the probabilistic surge hazard under sea level rise. For example, vegetation can attenuate the waves (Augustin et al., 2009) and potentially slow the erosion of coastal dunes (Collins et al., 2004), while seawater intruding into fresh water, may lead to die off of fresh marsh and a corresponding reduction of vegetative flow resistance (Bilskie et al., 2014; Smith et al., 2010). Projection of coastal evolution is complex and is out of the scope of this paper. However, we conduct a sensitivity test to better understand the potential impact of barrier island evolution on the surge hazard in Sarasota Bay because of the large surge-SLR

nonlinearity here.

Longboat Key, the long narrow barrier island stretching from northwest to southeast in front of Sarasota Bay, has an average sea-front dune crest height of about 3 m. Most of these dunes have dense vegetation on the top. One way to indirectly but simply investigate how dune degradation on Longboat Key will affect surge response to SLR is to investigate how lowered dune heights and loss of dune vegetation affect nonlinearity. The tropical cyclone contributing the most probability to the 1% AEP surge value in the study area is selected for this sensitivity analysis. The selected storm (central pressure deficit 47 hPa, storm size 39 km, forward speed 12 m/s, landfall just north of Tampa Bay) is simulated for all four SLR scenarios, both on the original mesh and the modified mesh with the whole island of Longboat Key lowered by 1 m but not less than 1 m (referred to as the lowered-dune-height mesh). If the lowered dune is submergent under any SLR scenario, the vegetation is moved as well. Surge profiles are plotted and compared for two transects across Longboat Key and Sarasota Bay for all simulations.

For both transects, lowered dunes on Longboat key slightly decrease surge height in front of Longboat Key and increase surge height for 0.2-0.5 m within Sarasota Bay for all SLR scenarios, which is expected because lower dunes mean less restrictions for surge water to flow into the bay. In most cases, i.e., for all the SLR scenarios along the south track and 0.65 m SLR scenario along the north track, nonlinearity (represented by DNL here) does not change markedly with lowered dunes. In contrast, for the 1.30 m and 1.95 m SLR along the north track near the opening of Tampa Bay, superlinearity decreases relatively significantly in Sarasota Bay, especially for the SLR 1.95 m scenario, for which the average decrease of the superlinearity is about 0.2 m for the selected tropical cyclones. This is most likely because with lowered dunes, due to northwesterly and onshore storm winds, more water can get into

the bay and accumulate around the north transect than the amount of water that can escape Sarasota Bay from the opening to Tampa Bay already under present-day scenario.

However, it should noted that barrier island erosion is an evolving process. In reality, the nonlinearity is more like comparing the original mesh present-day surge and the lowered-dune-hight mesh surge with SLR. In this way, the superlinearity is always higher when considering dune erosion, and can be as large as 1.5 m within Sarasota Bay in this sensitivity test.

It is noteworthy that the erosion case presented here is an extreme case and unlikely to happen. Longboat Key is also a highly developed area with beach nourishment projects and other engineering protection measures, which make any prediction of Longboat Key's long-term morphological evolution difficult. The implication of this sensitivity test is nevertheless the importance of engineering the barrier island to keep it functional to block surge under future sea level rise scenarios.

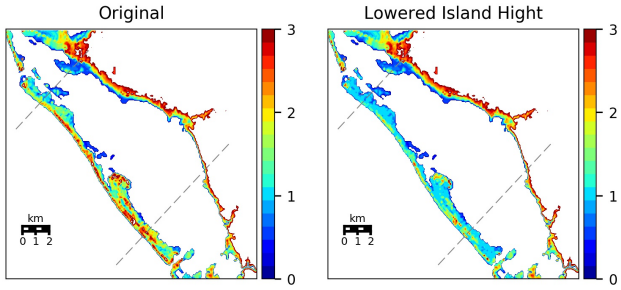

Figure B.1: Longboat Key topography in the original mesh and modified mesh with lowered dune heights. Dashed gray lines represent transects across Sarasota Bay

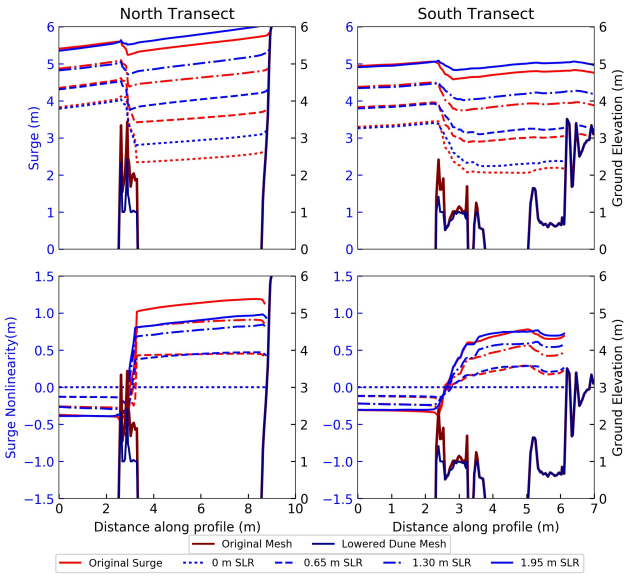

Figure B.2: Surge and surge nonlinearity profiles along two transects across Sarasota Bay for selected tropical cyclones on the original mesh and the lowered-dune mesh.

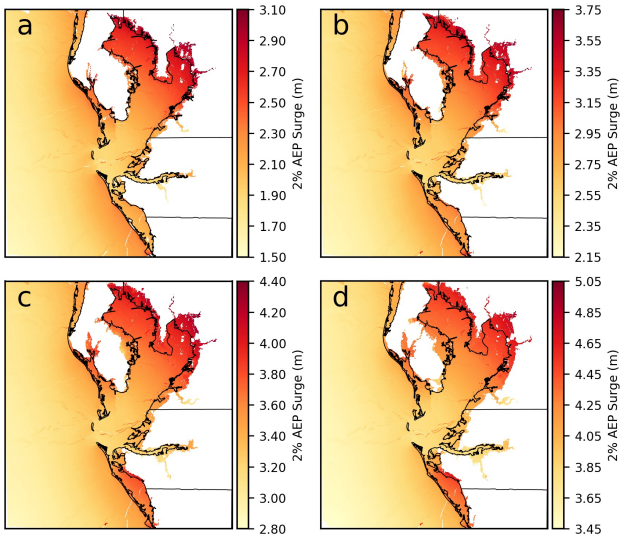

Figure B.3: 2% AEP probabilistic surge hazard maps calculated from 188 tropical cyclones under four SLR scenarios: a) present-day, b) 0.65 m, c) 1.30 m, and d) 1.95 m. The color bars are selected so that the same color in each map represents a perfectly linear surge-SLR response, i.e., the probabilistic surge with SLR will be the exact summation of the two.

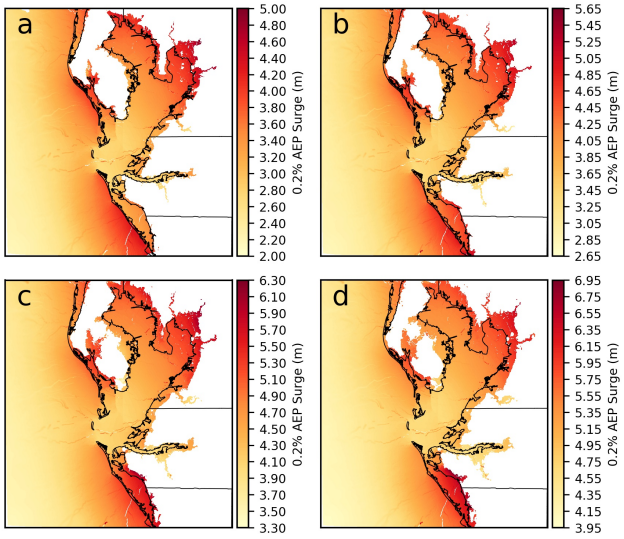

Figure B.4: 0.2% AEP probabilistic surge hazard maps calculated from 188 tropical cyclones under four SLR scenarios: a) present-day, b) 0.65 m, c) 1.30 m, and d) 1.95 m. The color bars are selected so that the same color in each map represents a perfectly linear surge-SLR response, i.e., the probabilistic surge with SLR will be the exact summation of the two.

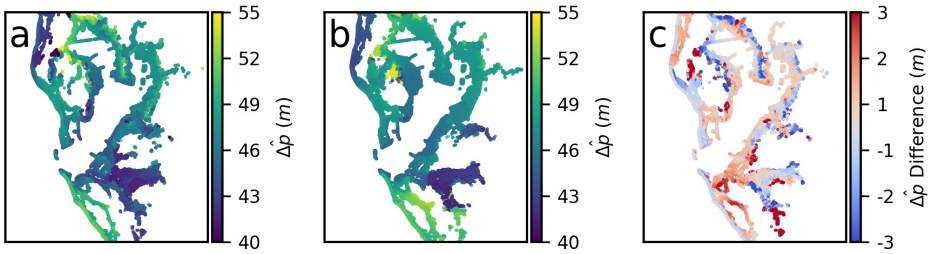

Figure B.5: 1% AEP Contribution-weighted mean value of pressure deficit at all locations of interest in the study area for a) present-day, b) 1.95 m SLR scenario, and c) the difference between the two.

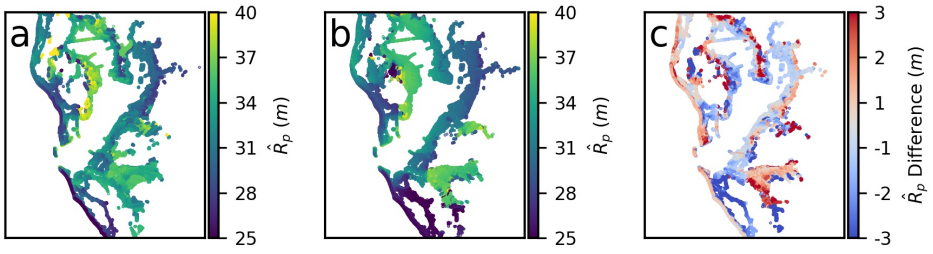

Figure B.6: 1% AEP Contribution-weighted mean value of pressure scale radius at all locations of interest in the study area for a) present-day, b) 1.95 m SLR scenario, and c) the difference between the two.

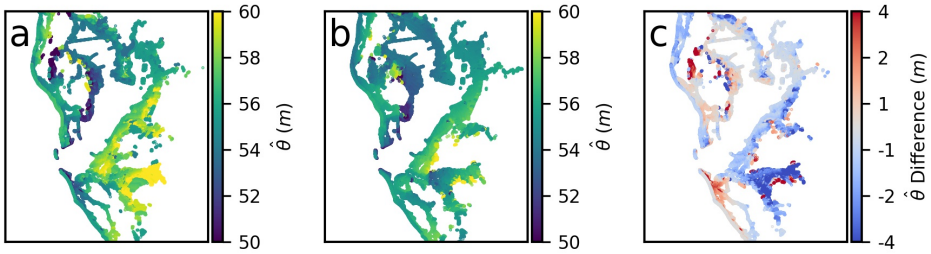

Figure B.7: 1% AEP Contribution-weighted mean value of heading at all locations of interest in the study area for a) present-day, b) 1.95 m SLR scenario, and c) the difference between the two. Decreasing of the contribution-weighted mean value of track approach angle around the Manatee river area indicates that while a more easterly moving storm gets more water up the Manatee river, the increase of sea level makes the Manatee river area act more like the coast, where a direct hit brings more surge.